



**HAL**  
open science

# Localized Afterslip at Geometrical Complexities Revealed by InSAR After the 2016 Central Italy Seismic Sequence

Lea Pousse-Beltran, Anne Socquet, Lucilla Benedetti, Marie-Pierre Doin,  
Magali Rizza, Nicola d'Agostino

► **To cite this version:**

Lea Pousse-Beltran, Anne Socquet, Lucilla Benedetti, Marie-Pierre Doin, Magali Rizza, et al.. Localized Afterslip at Geometrical Complexities Revealed by InSAR After the 2016 Central Italy Seismic Sequence. *Journal of Geophysical Research: Solid Earth*, 2020, 125 (11), 10.1029/2019JB019065 . hal-03027096

**HAL Id: hal-03027096**

**<https://hal.science/hal-03027096>**

Submitted on 27 Nov 2020

**HAL** is a multi-disciplinary open access archive for the deposit and dissemination of scientific research documents, whether they are published or not. The documents may come from teaching and research institutions in France or abroad, or from public or private research centers.

L'archive ouverte pluridisciplinaire **HAL**, est destinée au dépôt et à la diffusion de documents scientifiques de niveau recherche, publiés ou non, émanant des établissements d'enseignement et de recherche français ou étrangers, des laboratoires publics ou privés.

1  
2  
3  
4  
5  
6  
7  
8  
9  
10  
11  
12  
13  
14  
15  
16  
17  
18  
19  
20  
21  
22  
23  
24

Title:

---

**Localized afterslip at geometrical complexities revealed by InSAR after the 2016 Central Italy seismic sequence**

Authors:

Léa Pousse-Beltran<sup>1</sup>, Anne Socquet<sup>2</sup>, Lucilla Benedetti<sup>1</sup>, Marie-Pierre Doin<sup>2</sup>, Magali Rizza<sup>1</sup>, Nicola D’Agostino<sup>3</sup>

<sup>1</sup> Aix Marseille Université, CNRS, IRD, Collège de France, CEREGE, Aix-en-Provence, France

<sup>2</sup> Université Grenoble-Alpes, Université de Savoie Mont-Blanc, CNRS, IRD, IFSTTAR, ISTerre, 38000 Grenoble, France

<sup>3</sup> Istituto Nazionale di Geofisica e Vulcanologia (INGV), Centro Nazionale Terremoti, via di Vigna Murata 605, 00143, Rome, Italy

Email list:

- Léa Pousse-Beltran: [pousse@cerege.fr](mailto:pousse@cerege.fr)
- Anne Socquet : [anne.socquet@univ-grenoble-alpes.fr](mailto:anne.socquet@univ-grenoble-alpes.fr)
- Lucilla Benedetti : [benedetti@cerege.fr](mailto:benedetti@cerege.fr)
- Marie-Pierre Doin : [marie-pierre.doin@univ-grenoble-alpes.fr](mailto:marie-pierre.doin@univ-grenoble-alpes.fr)
- Magali Rizza : [rizza@cerege.fr](mailto:rizza@cerege.fr)
- Nicola D’Agostino : [nicola.dagostino@ingv.it](mailto:nicola.dagostino@ingv.it)

25 Keywords:

- 26 - Postseismic
- 27 - InSAR time-series
- 28 - 2016-2017 Amatrice-Norcia Seismic Sequence
- 29 - Geometrical complexity

30

31 Key points:

- 32 - We monitor pre and post-seismic deformation of the 2016 seismic sequence using two-
- 33 year InSAR time-series
- 34 - Centimetre scale post-seismic surface displacements are detected after October 30,
- 35 2016 Mw 6.5 mainshock (Norcia earthquake)
- 36 - Localized shallow afterslip occurred at structural complexity that may have hindered
- 37 the propagation of seismic ruptures

38

39

40 **Abstract :**

41         The Mw 6.5 Norcia earthquake occurred on October 30, 2016, along the Mt Vettore  
42 fault (Central Apennines, Italy), it was the largest earthquake of the 2016-2017 seismic  
43 sequence that started two months earlier with the Mw 6.0 Amatrice earthquake (August, 24).  
44 To detect potential slow slip during the sequence, we produced Interferometric Synthetic  
45 Aperture Radar (InSAR) time-series using 12 to 6-day repeat cycles of Sentinel-1A/1B images.  
46 Time-series indicates that centimetre-scale surface displacements took place during the 10  
47 weeks following the Norcia earthquake. Two areas of subsidence are detected: one in the  
48 Castelluccio basin (hanging wall of the Mt Vettore fault), and one in the southern extent of the  
49 Norcia earthquake surface rupture, near an inherited thrust. Poroelastic and viscoelastic  
50 models are unable to explain these displacements. In the Castelluccio basin, the displacement  
51 reaches  $13.2 \pm 1.4$  mm in the ascending line of sight (LOS) on January 06, 2017. South of the  
52 Norcia earthquake surface rupture (a zone between the Norcia and Amatrice earthquakes),  
53 the post-seismic surface displacements affect a smaller area, but reach  $35.5 \pm 1.7$  mm in  
54 ascending LOS by January 2017 and follow a logarithmic temporal decay consistent with post-  
55 seismic afterslip. Our analysis suggests that the structurally complex area located south of the  
56 Norcia rupture (30 October) is characterized by a conditionally stable frictional regime. This  
57 geometrical and frictional barrier likely halted rupture propagation during the Amatrice  
58 (August 24) and Norcia (October 30) earthquakes at shallow depth (<3-4 km).

59

## 60 1 Introduction

61 Monitoring the spatial and temporal variations of the slip on a fault enables researchers  
62 to better assess stress build-up on seismic asperities and slip released during seismic cycle  
63 (Avouac, 2015; Bürgmann, 2018; Chen & Bürgmann, 2017; Harris, 2017). In the rate and state  
64 formulation, rupture propagation can be hindered by rate-strengthening sections of a fault,  
65 which tend to slip via creep rather than in seismic rupture (e.g., H. Perfettini et al., 2010; Hirose  
66 et al., 2010). Such barriers are also often associated with structural complexities – such as a  
67 change of strike, secondary faulting or interaction with inherited faults (e.g., King & Nabelek,  
68 1985; King, 1986; Wesnousky, 1988). These structural complexities can act as a geometrical  
69 barrier, and are characterized by an increased equivalent strength (Nielsen & Knopoff, 1998).  
70 Locating aseismic slip on the fault and comparing these locations with those of seismic slip and  
71 fault segmentation is of pivotal importance to better characterize the frictional behavior of a  
72 fault system and its relation with structural complexities.

73 A notable seismic sequence occurred in the Central Apennines (Italy) in 2016-2017  
74 (Chiarabba et al., 2018; Perouse et al., 2018; Cheloni et al., 2017; Huang et al., 2017; Cirella et  
75 al., 2018; Civico et al., 2018; Scognamiglio et al., 2018; Ragon et al., 2019), with four main  
76 events: the 24<sup>th</sup> August 2016  $M_w$  6.0 Amatrice event, the 26<sup>th</sup> October 2016  $M_w$  5.9 Visso  
77 event, the 30<sup>th</sup> October 2016  $M_w$  6.5 Norcia event, and the 18<sup>th</sup> January 2017  $M_w$  5.5  
78 Campotosto event (Figure 1 and Table S1). This seismic sequence ruptured the complex Mt  
79 Vettore fault system (in red in Figure 1) (Pizzi et al., 2017; Porreca et al., 2018; Villani, Pucci, et  
80 al., 2018), and the adjacent Amatrice-Campotosto fault (in orange in Figure 1). During the  
81 Norcia earthquake, the rupturing of an antithetic fault on the opposite side of the Castelluccio  
82 basin seems necessary to fit geodetic data and is supported by alignments of relocated  
83 aftershocks (Chiaraluce et al., 2017; Walters et al., 2018; Cheloni et al., 2019). In addition, the  
84 role of an inherited west-dipping thrust called OAS (Olevano-Antrodoco-Sibillini thrust) in the  
85 Norcia earthquake coseismic rupture geometry has been widely discussed. While some studies  
86 suggested that only the Mt Vettore fault system was activated (Chiaraluce et al., 2017; Liu et  
87 al., 2017; Papadopoulos et al., 2017; Pavlides et al., 2017; Pizzi et al., 2017; Wang et al., 2018;  
88 Xu et al., 2017), others suggested that also the OAS thrust ruptured as a reactivated high-angle  
89 normal fault during the event, as suggested by geodetic and seismological observations  
90 (Cheloni et al., 2017; Scognamiglio et al., 2018; Walters et al., 2018). Although the reactivation  
91 of the thrust is not clearly demonstrated (Cheloni et al., 2019), the OAS appears to have played

92 a role in the aftershock distribution (Chiarabba et al., 2018; Chiaraluca et al., 2017; Pizzi et al.,  
93 2017). The earthquakes of the 2016 sequence appear to have nucleated near crosscutting  
94 structures that seem to have been loaded by previous ruptures in the sequence (Chiaraluca et  
95 al., 2017; Pino et al., 2019). This seismic sequence is thus an excellent case study to better  
96 understand the link between structural segmentation, aseismic slip and frictional properties  
97 that might control this rupture propagation.

98 Post-seismic processes during this sequence have been observed in the seismicity (e.g.,  
99 Albano et al., 2018; Tung & Masterlark, 2018), but no aseismic slip has been detected with  
100 geodetic data so far. Using Interferometric Synthetic Aperture Radar (InSAR) time-series from  
101 Sentinel-1 data, we document a small but significant post-seismic deformation transient that  
102 we find is best explained by aseismic slip on faults associated with this sequence. Surface  
103 displacements are presented and analysed. We also explore simple modelling schemes that  
104 provide a framework for our interpretation and discussion.

## 105 2 Geological setting

106 The Central Apennines were affected by an extensional phase during the Jurassic,  
107 followed by a compressive phase during the Neogene (e.g., Calamita et al., 2011). The OAS  
108 (Olevano-Antrodoco-Sibillini thrust) is one the main thrusts resulting from the Neogene  
109 compressive phase (Calamita et al., 1994) and has been interpreted as a transpressive ramp  
110 (Di Domenica et al., 2012). In the area affected by the 2016-2017 seismic sequence, the OAS  
111 thrust is expressed by parallel splays associated with fault-bend folds characteristic of  
112 structural ramps (Calamita et al., 2012) (Figure 1). The ongoing ENE oriented extension of 2  
113 to 4 mm/yr (D'Agostino, 2014; Carafa & Bird, 2016; Devoti et al., 2017), which probably began  
114 in the Early Pleistocene (e.g., Galadini & Galli, 2000), is currently accommodated through  
115 normal fault systems such as the Monte Vettore fault system that hosted the 2016-2017  
116 seismic sequence.

117

## 118 3 Surface displacements during the seismic sequence

### 119 3.1 InSAR processing

120 Synthetic radar interferometry (InSAR) is now systematically used to constrain  
121 deformation fields (Elliott, Walters, et al., 2016) and can document centimetre to millimetre  
122 scale slow aseismic ground deformation using an adapted processing chain (Hussain et al.,

123 2018; Aslan et al., 2019). We used C band (5.5 cm wavelength) images from Sentinel-1A/B  
124 images (Figure 1-A) spanning almost two years (July 28, 2015, to June 11, 2017) for the  
125 ascending track (A117, subswath IW3). To confirm the main observations made on the  
126 ascending track, we processed descending track (D22, subswaths IW2 and IW3) images from  
127 October 26, 2016 to February 11, 2017. SAR images were processed in VV polarization. We  
128 used the NSBAS processing chain (Doin et al., 2011, 2015) modified for Sentinel data by  
129 Grandin (2015) to generate differential interferograms. The interferogram network, and  
130 examples of unfiltered and uncorrected interferograms, are provided in Figures S1 and S2. The  
131 Shuttle Radar Topography Mission digital elevation model (DEM) at 3 arc sec resolution (Rabus  
132 et al., 2003), resampled at 45m resolution, has been used to accurately coregister the focused  
133 SAR images and to correct interferograms from the topographic contribution to the  
134 interferometric phase. We removed a ramp in range and in azimuth for each interferogram  
135 using the methodology of Cavalié et al., (2007) included in NSBAS. We de-noised the  
136 interferograms before unwrapping using collinearity, a criterion to characterize at each pixel  
137 the local spatial variability of the phase (Pinel-Puységur et al., 2012). The collinearity was used  
138 to adapt the strength of the filter. We filtered for a window of 12 pixels (400m in range and  
139 700m in azimuth); the filter is described in Doin et al. (2011) and is based on the collinearity  
140 value which weights the complex phase in a sliding window. For the filter we had the option  
141 of adapting the weighting of the phase within windows of different sizes. This size adaptation  
142 depends on the collinearity within the windows. Unwrapping was performed in 2D with the  
143 NSBAS chain (Grandin et al., 2012; Doin et al., 2015). After unwrapping, to account for errors  
144 associated with stratified troposphere, we removed a quadratic cross-function of elevation ( $z$ )  
145 and azimuth to ramps in azimuth ( $y$ ) and in range ( $x$ ) estimation following the function  
146  $ax+by+c+ez+fz \times az+g \times (z \times az)^2$  using a least-square approach (Daout et al., 2019). Time-series  
147 were then calculated following the NSBAS method (Doin et al., 2011; Daout et al., 2016) using  
148 an approach based on the Small Baseline Subset time-series Analysis (SBAS) of López-Quiroz  
149 et al., (2009)'s algorithm. The smoothing of the pixel time-series is performed by minimizing  
150 the Laplacian of the temporal evolution of the deformation (Cavalié et al., 2007). The final pixel  
151 size is 62 m in azimuth and 37 m in range. We removed pixels with an RMS value greater than  
152 0.7. For the ascending track, we build a time series spanning the 2 years (from 28/07/2015 to  
153 11/06/2017 ) (Figure S1 and see missing links in the time series in Figure S3). For this complete  
154 2-year time-series, we encounter problems in unwrapping the co-seismic interferograms due

155 to the large deformation with respect to the Sentinel wavelength in near field (aliasing).  
156 Fringes are too close in space and cannot be unwrapped. At pixels that are incoherent in the  
157 co-seismic interferogram (i.e. in near field), this causes gaps in the complete (2 yrs) time-series  
158 spanning the main earthquakes (Norcia, Amatrice and Campotosto earthquakes) (Figure S3),  
159 or lead to an underestimation of the coseismic displacement (brown circles in Figure 2-D). In  
160 addition, we also build three time-series in between earthquakes in order to avoid possible  
161 bias: before the 24<sup>th</sup> August (Amatrice earthquake), between 27<sup>th</sup> August and 26<sup>th</sup> October  
162 (between the Amatrice and Visso earthquake), and after the 30<sup>th</sup> October (Norcia earthquake).  
163 We excluded the SAR data from January 18, 2017, which produced noised interferograms. For  
164 the descending track, we build two time-series: between 27<sup>th</sup> August and 26<sup>th</sup> October (Visso  
165 earthquake), and after the 30<sup>th</sup> October (Norcia earthquake).

## 166 3.2 Time-series results and description of the main features

### 167 3.2.1 Ascending Track

168 The ascending time-series built before the seismic sequence (from July 28<sup>th</sup> 2015 to  
169 August 21<sup>th</sup> 2016) does not show significant nor localized surface displacements along the  
170 main faults (Figure S4-A,B). After October 30<sup>th</sup>, the (post-Norcia) time-series shows  
171 centimetre-scale displacements going away from the satellite in the LOS direction in three  
172 areas (Figure 2-B):

- 173 • South of Amatrice: In the area affected by the Campotosto earthquake (January  
174 18<sup>th</sup>, 2017 Mw 5.0 -5.5 EQ) the ground surface moved away from the satellite by  
175 more than 60 mm in LOS (Figure 2-B). This coseismic displacement results in a step  
176 function in the time series, and can therefore be easily separated from any gradual  
177 post-seismic deformation.
- 178 • Near Arquata del Tronto: At the southern extremity of surface rupture of the Mw  
179 6.5 October 30<sup>th</sup> Norcia earthquake (red faults in Figure 2), surface displacements  
180 are detected over an area of  $\sim 12 \text{ km}^2$ , and follow logarithmic evolution (in Figure  
181 2-D and Figure 3-A see time-series at point 1 where the cumulative post-Norcia  
182 displacements in LOS on January 06, 2017 is in average  $\sim 35.5 \pm 1.7 \text{ mm}$  and reach  
183  $50.5 \pm 2.1 \text{ mm}$  on 30 April 2017)
- 184 • Castelluccio Basin: On the hanging wall of the Mt Vettore fault, slow deformation  
185 affects an area of  $\sim 50 \text{ km}^2$  (Figure 2), and is associated with displacements in the

186 LOS direction that are  $13.2 \pm 1.4$  mm in average at Point 2 on 6 January and reach  
187  $37.9 \pm 1.3$  mm on 30 April 2017 (Figure 2-D and Figure 3-A).

188 To rule out possible bias due to the Campotosto earthquakes affecting the area near  
189 Castelluccio and near Arquata del Tronto, we confirmed these previous observations with a  
190 shorter time-series calculated between the Norcia and Campotosto earthquakes (November  
191 1<sup>st</sup> – January 12<sup>th</sup>) (Figure 4). We prefer to use, for the rest of the manuscript, the longer post-  
192 Norcia time-series (November 1<sup>st</sup> – June 11<sup>th</sup>) that shows a better signal-noise ratio.

193 In the post Amatrice earthquake time series (August 27 to October 26) we did not observe  
194 any localized surface displacements similar to the pattern observed after October 30 (Norcia  
195 earthquake) (Figure S4-B). Yet near the town of Amatrice, we observe diffuse surface  
196 displacements ( $< \sim 2.5$  cm) moving away from the satellite. However, this time-series is  
197 constrained by only 9 scenes and 20 interferograms, which prevents from properly (i)  
198 constraining a low amplitude signal and (ii) correcting for atmosphere and topography. The  
199 surface displacements here have a low signal to noise ratio. The variance of the uncorrelated  
200 noise is  $\sim 40$  mm<sup>2</sup> (see Supplementary Text S1 and Figure S5-A), and the standard deviation  
201 sigma of the noise is thus 6.3 mm. We take  $3 \cdot \text{sigma} = 20$  mm to set our limit of detection. The  
202 characteristic length scale of correlated noise is 5.0 km and there is autocovariance for  
203 distances smaller than  $\sim 15$  km (see Figure S5-A). Observed patterns cannot be differentiated  
204 from noise, analyses on SAR images from other satellites should be carried out to confirm or  
205 not the post-Amatrice (August 24 earthquake) surface displacements.

### 206 3.2.2 Descending Track

207 To confirm the post-October 30 (Norcia earthquake) observations we processed  
208 descending interferograms (Figure 2-C). We used a 3-month dataset for the descending track  
209 (November 1st, 2016 to February 11, 2017). Time-series calculated for the descending track  
210 also indicate slow deformation after Norcia earthquake (October, 30), that reaches on average  
211  $20.5 \pm 2.7$  mm on January 24 in the LOS direction near Arquata del Tronto (point 1). The  
212 deformation reached on average  $10.8 \pm 1.5$  mm in the Castelluccio basin (in point 2). Assuming  
213 negligible north-south displacements, by combining the results from ascending and  
214 descending tracks, the displacement is dominated by subsidence in this area (Figure S6).

215 In the first order, deformation observed in the descending track is compatible with  
216 results inferred from the ascending track. Noise and unwrapping issues led us to mask noisy  
217 areas and resulted in more blank pixels in the descending track picture which should be used

218 with caution. The relief projected in the descending LOS geometry masked a ridge (Mt Bove -  
219 Mt Vettore – Mt Gorzano high massifs) (Figure S7). In addition to noise, this resulted in an  
220 incoherent area and made unwrapping difficult in that area. The temporal evolution of the  
221 features slightly differs from the one in the ascending track. The removal of the 7<sup>th</sup> November  
222 SAR images (affected by strong atmosphere conditions) and the poor constraint on the 19<sup>th</sup>  
223 November SAR images (see the network in Figure S1) could affect the time-series in November.  
224 Falcucci et al. (2018) had similar difficulties in using descending SAR images to survey the  
225 January 2017 Campotosto seismic event. This might be due to the early morning acquisition  
226 time, which amplifies decorrelation due to change of moisture level or thawing.

227 In addition, we produced time-series calculated between the Amatrice and Norcia  
228 earthquakes. This time-series is also affected by a short-wavelength atmospheric turbulence  
229 that makes it difficult to interpret (Figure S5-B-C). The variance of noise is  $\sim 21 \text{ mm}^2$ . The  
230 characteristic length scale of correlated noise is 5.0 km and there is autocovariance for  
231 distances smaller than  $\sim 15 \text{ km}$  (see Figure S5). Again, displacement less than 19 mm for the  
232 ascending track and under 14 mm for the descending track, cannot be considered as  
233 detectable signal, therefore constraining smaller surface displacements between the Amatrice  
234 and Norcia events demands complementary time-series with SAR images from other satellite.

### 235 3.2.3 Comparison with GNSS

236 Few GNSS stations exist near the studied area (ARQT, LNSS see station locations in Figure  
237 2-A). Those GNSS time-series agree with InSAR time-series sampled at the same locations  
238 (Figure S8).

### 239 3.3 Pattern temporal evolution

240 By sampling the time-series, the temporal evolution is shown by averaging pixel  
241 displacement in area. To enhance the precision of the displacement temporal evolution  
242 without using time-series inversion, we temporally track a stable pattern in our unwrapped  
243 interferograms (Grandin, 2009). The method is detailed in Supplementary Text S2 and is  
244 illustrated by Figures S9-S10.

245 This method can only be used on areas where the displacement pattern is well defined,  
246 and works well in our case to track the evolution of the area near Arquata del Tronto (pattern  
247 in Figure 4 which encompasses the point 1). After the Norcia earthquake, the amplitude ratio  
248 is higher, and a logarithmic decay is clearly identified there (Figure 3-B). The pattern tracking  
249 shows a temporal evolution similar to the averaging surface displacement method. We are

250 therefore confident that pixel averaging adequately captures the evolution of displacement  
251 that we want to describe. For the descending interferograms, the pattern is not precisely  
252 trackable and its time evolution is noisy (grey curve in Figure S10-C). This could be due to a  
253 poor correlation for the pattern in some interferograms. The evolution of the pattern around  
254 Castelluccio Basin (pattern in Figure 4) is poorly resolved too.

## 255 4 Modelling 3D deformation field

### 256 4.1 Comparison with topography and geology

257 To interpret the displacement pattern near Arquata del Tronto we compared it with the  
258 topography and the geology. There is no correlation with either the slope or the relief (Figure  
259 S11), thus we can exclude a gravitational process (i.e. landslide) as an explanation for the  
260 observed displacements. Concerning geology, the OAS thrusts fractured Meso-Cenozoic  
261 carbonate rocks over Neogene pelagic sediments; the carbonates host some of the largest  
262 aquifers in the Apennines while the Neogene sediments are thought to be an aquiclude (Figure  
263 S12) (Boni et al., 2010). The OAS delimiting these two units therefore acts as an impermeable  
264 boundary (Boni et al., 2010). Petitta et al., (2018) and Valigi et al., (2019) show that the 2016-  
265 2017 Italian seismic sequence had effects on spring discharge, water-table levels, and  
266 streamflow of those aquifers. In our results, the extent of the Maiolica unit, which hosts a  
267 shallow aquifer (Boni et al., 2010), corresponds well with the deformation area near Arquata  
268 del Tronto (Figure S11-A-B). The long pre-seismic InSAR time-series did not show any seasonal  
269 deformation in this aquifer, which means that groundwater seasonal processes can be  
270 excluded (point 1 in Figure 2-D). In addition, it seems difficult to get more than 1 cm of  
271 subsidence from winter rain in this area (i.e., Silverii et al., 2016).

### 272 4.2 Poro-elastic modelling

273 Poro-elastic effects have been studied during the 2016-2017 seismic sequence to explore  
274 the aftershocks and earthquakes triggering. Tung & Masterlark (2018) suggest that fluid  
275 migration caused by the Amatrice earthquake (August 24, 2016) could have triggered the Visso  
276 earthquake (October 26, 2016), as well as some associated aftershocks. They inferred that this  
277 poro-elastic triggering should have occurred in an intermediately fractured crust. They also  
278 estimated that afterslip and viscoelastic-relaxation were quite negligible with respect to  
279 poroelastic effects. Albano et al. (2018) also suggest that post-seismic fluid diffusion after the  
280 Amatrice earthquake is related to aftershocks. According to their pore fluid diffusion model,  
281 there could be some associated afterslip (~ 10 cm) after the Amatrice earthquake.

282 The Maiolica karst aquifer is shallow and unconfined but Roeloffs (1996) postulates that  
283 every aquifer reacts as a confined aquifer to a disturbance at short timescale. Here, to compare  
284 with the displacement pattern near Arquata del Tronto, we thus test a forward model of poro-  
285 elastic rebound using Relax software (Barbot & Fialko, 2010). We perform a simple poro-elastic  
286 model with no lateral variation of diffusivity, that does not account for the spatially  
287 heterogeneous distribution of local aquifers. We use the slip distribution models of the Norcia  
288 and Visso mainshocks (Maubant et al., 2017), (Figure S13 and Figure 5–A). We do not take into  
289 account the Amatrice earthquake since poroelastic rebound from the Amatrice earthquake  
290 would likely have stabilized by the time of the Visso and Norcia earthquakes (Figure 4-f in  
291 Albano et al., (2018)). We tested several diffusivities for a shallow layer (0-5 km depth), from  
292 1.5 m<sup>2</sup>.s proposed by the Tung and Masterlark (2018)’s aftershocks analysis to 10<sup>4</sup> m<sup>2</sup>/s  
293 (maximum diffusivity value for karst) (Roeloffs, 1996). Other parameters are described in detail  
294 in Figure 5. This model predicts uplift in the Castelluccio Basin and near Arquata del Tronto  
295 (Figure 5-D) where we observe subsidence (Figure 5-C). This discrepancy allows us to rule out  
296 poro-elastic rebound as the main driver of observed deformation. These poroelastic models  
297 are not exhaustive, we only explore simple geometrical configurations using parameter values  
298 informed by the local geology, however, other karstic configurations would likely predict uplift  
299 as well.

#### 300 4.3 Viscoelastic modelling

301 Viscoelastic relaxation in the crust and in the mantle is also an important aseismic  
302 process, and has been inferred to be the driver of post-seismic deformation following many  
303 earthquakes (e.g., Pollitz et al., 2001; Zhao et al., 2017). To test whether viscoelastic relaxation  
304 is a plausible driving mechanism for post-Norcia deformation, we used Relax to perform  
305 forward modelling in a simple layered framework. Our model uses the stress perturbation  
306 from the three mainshocks: the Amatrice earthquake using the slip distribution of Ragon et  
307 al., (2019) added to the Visso and Norcia earthquakes using the slip distribution model of  
308 Maubant et al., (2017). We set the upper, middle and lower crust thickness to the values  
309 proposed in Laske et al., (2013) and Verdecchia et., al. (2018) (see Table 1). We tested a  
310 viscoelastic relaxation governed by a Newtonian rheology with  $\dot{\gamma} = \frac{\tau}{\eta}$  where  $\dot{\gamma}$  is the viscous  
311 strain rate,  $\tau$  is the deviatoric stress and  $\eta$  is the Newtonian viscosity. We used viscosity values  
312  $\eta$  inferred in studies of viscoelastic relaxation modelling using GPS measurements following  
313 1997 Umbria-Marche earthquakes, or using levelling line measurements following the 1915

314 Fucino earthquake (Amoruso et al., 2005; Aoudia et al., 2003; Riva et al., 2007). These studies  
315 inferred that the ductile structure of the Central Apennines consists of an elastic upper crust  
316 overlaying a middle crust ( $10^{18}$ - $10^{19}$  Pa s), a viscous lower crust ( $10^{17}$ - $10^{18}$  Pa s) and the upper  
317 mantle ( $10^{21}$  Pa s) (Table 1).

318 Although those models are geometrically simple and do not take into account  
319 earthquakes prior 2016, they predict at a long-wavelength uplift (>50 km) in the area where  
320 we observe subsidence (Figure 6). This discrepancy in both sign and wavelength allows us to  
321 rule out a simple visco-elastic relaxation as the main driver of observed deformation. Visco-  
322 elastic models are not exhaustive here: nonlinear viscoelastic rheologies (e.g., power law  
323 creep) in lower crust (Freed & Bürgmann, 2004) could also be investigated; however finite  
324 element models with creeping lower crust seem also to predict uplift in similar settings of  
325 normal fault systems (e.g., Thompson & Parsons, 2016). It is worth also mentioning that the  
326 observed logarithmic decay could also potentially be associated with Burgers rheology or shear  
327 zone (e.g., Hetland & Zhang, 2014) and could also be investigated in future work. Although, as  
328 with the poroelastic modeling, it seems unlikely that a different geometry or rheology could  
329 completely reverse the sign of uplift and subsidence (for example, a different rheology would  
330 only affect the temporal evolution/spatial distribution).

#### 331 4.4 Modelling the temporal evolution of afterslip

332 The logarithmic-like temporal evolution of displacement (Figure 3-A), and the  
333 disagreement between the observations and the predictions of poroelastic and viscoelastic  
334 models, suggest that afterslip may have been the main driver of postseismic deformation  
335 (Marone et al., 1991). Thus to characterize the temporal evolution of the deformation, we  
336 fitted the deformation decay (of the raw time-series and of the pattern tracking evolution)  
337 with the logarithmic function (Figure 3-A-B respectively) from the Marone et al. (1991) model  
338 and Zhou et al. (2018) reformulation for rate-strengthening afterslip:

$$339 \quad U(t) \approx \alpha \times \ln(1 + c \times t)$$

$$340 \quad c = \frac{\beta \times V_i}{\alpha}$$

341 In which U: afterslip in time t,  $\alpha$ : characteristic length scale,  $\beta \times V_i$  : initial rate at the  
342 beginning of the post-seismic period, with  $\beta$  a scaling vector by which the sliding rate evolves  
343 in response to the stress and  $V_i$  the pre-seismic slip rate.

344 At point 1 (near Arquata del Tronto), the good fit of the afterslip model suggests that the  
345 main post-seismic process is likely an afterslip phenomenon. Since we found similar results for  
346  $c$  value (describing the temporal decay) using the raw pixel time series and using the pattern  
347 tracking (independent for the time-series inversion), we are confident in our fitting (Table 2).  
348 The first post-Norcia Sentinel image has been acquired 2.6 days after the Norcia earthquake;  
349 therefore those 2.6 days of early afterslip are missing in our data. We compare the temporal  
350 decay of the deformation with the cumulative moment and number of aftershocks (blue and  
351 green curves in Figure S14). Although the completeness magnitude is high (ML 3 in Figure S5  
352 in Chiaraluce et al., (2017)), those two curves obtained with less than 50 events are not  
353 following the same trends, aftershocks do not seem to be induced by afterslip. At point 2 (near  
354 Castelluccio di Norcia), the temporal decay does not fit with the afterslip law as the rate at the  
355 beginning of the post-seismic period is close to zero ( $c$  value for the purple curve fit in Figure  
356 3-A). Other post-seismic processes could be a complementary driver of the deformation here  
357 and should be taken into account in further modelling (i.e. finite element forward model  
358 accounting for afterslip superimposed with poro-elastic rebound and viscoelastic relaxation).

## 359 4.5 Afterslip modelling on faults

### 360 4.5.1 Inversion strategy and fit to the data

361 To obtain the afterslip distribution we use the Classic Slip Inversion (CSI) Python tools  
362 (Elliott, Jolivet, et al., 2016; Jolivet et al., 2015) to invert for the slip. We use the constrained  
363 least-squares formula of Tarantola (2005) to solve the inverse problem (see details in  
364 Supplementary Text S3 and Figures S15 to S18). We chose a dip of  $40^\circ$  for the Mt Vettore fault  
365 (as Cheloni et al., (2017) see Figure S15) and project the fault down dip from the mapped fault  
366 at the surface (modeled fault geometry in yellow Figure 2-A). We discretize the fault into 88  
367 rectangular patches. The smoothed cumulative surface displacement on February 11, 2017,  
368 measured in both ascending and descending tracks are inverted to obtain the afterslip  
369 distribution. The resolution is good for short-wavelength features at shallow depths (<5 km  
370 depth) (Figure S16). As several geometries have been used to model the mainshock rupture  
371 (OAS reactivation, antithetic fault), we explored three cases: (1) slip only on the Mt Vettore  
372 Fault, (2) slip on the Mt Vettore Fault and on the OAS and (3) slip on the Mt Vettore Fault and  
373 an antithetic fault with a geometry similar to the one proposed by Cheloni et al., (2019) and  
374 Maubant et al., (2017) (dip  $65^\circ$ ) (Figures S17 to S20). We also explored the rake: (1) dip-slip  
375 only and (2) variable rake. A rigorous statistical comparison between the cases is difficult due

376 to variation in model parameters and number of degrees of freedom, as explained by Cheloni  
377 et al., (2019). We thus used the RMS values to compare the different cases. Here the case that  
378 reduces the residuals the most is the inversion with an antithetic fault. This case is in addition  
379 consistent with geological and seismological observations (i.e. Cheloni et al., 2019). The  
380 different cases were compared using the RMS (root mean square), and allows us to choose the  
381 inversion with an antithetic fault (Table S2).

382 Both ascending and descending tracks are well modelled (Figure 7). It is worth noting  
383 that the resolution is low at depth (Figure S16). The total geodetic moment released by the  
384 afterslip model is equivalent to  $M_w \sim 5.78$  (without taking into account the Campotosto  
385 earthquake) which corresponds to  $\sim 8.7\%$  of the geodetic moment released during the Norcia  
386 earthquake ( $M_w 6.5$ ).

387

#### 388 4.5.2 Afterslip distribution

##### 389 4.5.2.1 Near Arquata del Tronto

390 We obtain a maximum afterslip of  $\sim 100$  mm below Arquata del Tronto at shallow depth  
391 (0- 2 km depth) (Figure 7 Figure 8). The shallow part depth  $< 3-4$  km toward the south is  
392 associated with very low coseismic slip for both the Norcia and Amatrice earthquakes and is  
393 located at the edge of the coseismic asperities. This is also consistent with an afterslip process:  
394 the afterslip is located where the slip gradient increased the shear stress on the unruptured  
395 portions. This feature has also been observed after the L'Aquila earthquake (D'Agostino et al.,  
396 2012). We calculate a geodetic moment released equivalent to  $M_w \sim 5.1$  in this area (patches  
397 above 2km depth and south of Arquata del Tronto). The cumulative moment released by the  
398 seismicity (Figure S14-D) at this date corresponds to  $\sim 2.0\%$  of the moment released by the  
399 afterslip model. The deformation is thus mainly aseismic.

400 Brozzetti et al., (2019) found some surface ruptures south of the 30<sup>th</sup> October Norcia  
401 rupture ( $42^\circ 47'N$  in their Fig. 1-C) mapped by Villani et al., (2018). The ruptures mapped by  
402 Brozzetti et al., (2019) are subtle and according to us may correspond to post-seismic  
403 deformation, as was observed after the L'Aquila earthquake (D'Agostino et al., 2012).

##### 404 4.5.2.2 Castelluccio Basin

405 We observe a maximum slip of  $\sim 170$  mm below Castelluccio at  $\sim 5$  km depth. Some  
406 afterslip overlaps with the coseismic rupture area, but not in the area of maximum coseismic  
407 slip (Figure 7). As also the shape of the measured time-series did not fit with the afterslip's law

408 (Figure 3-A), a sole afterslip process is unlikely. It is possible that poroelastic and fluid flow  
409 processes could be at work here since there is a large basal aquifer (Boni et al., 2010).  
410 Modelling accounting for both processes could be performed, for example fully coupled  
411 poroelastic finite element numerical modelling with spatially variable material properties (e.g.,  
412 Albano et al., 2017).

## 413 5 Discussion

### 414 5.1 Afterslip mechanism near Arquata del Tronto

415 Based on Dietrich (1979), Ruina (1983) and Marone et al., (1991) equations, we  
416 estimated  $\alpha$  (the characteristic length scale over which the elastic stress changes by order of  
417 the frictional stress) in Figure 3 and Table 2. We can now estimate the friction  
418 parameter  $(a - b)$  since according to Perfettini and Avouac (2004) and Zhou et al., (2018):

$$419 \alpha = \frac{(a - b) \times \sigma}{k}$$

420

421 with  $k$ : the effective stiffness, and  $\sigma$  the effective normal stress. This relation can be applied  
422 to our case since the duration of our analysis ( $\sim 200$  days) is much shorter than the  
423 characteristic time  $t_d$  (Gualandi et al., 2014). Where  $t_d = \frac{\alpha}{V_{pl}}$  ( $> 12$  years) where  $V_{pl}$  is the local  
424 plate loading rate ( $< 2.1$  mm/yr (Puliti et al., 2020)). The fit to the displacement of the time-  
425 series sampled in point 1 by an afterslip law (Figure 3) leads to  $\alpha = 30.9 \pm 4.0$  mm. To estimate  
426  $\sigma$ , we assume that the mean normal stress may vary from the hydrostatic to lithostatic  
427 pressure, with a rock density of  $2.5 \text{ kg.m}^{-3}$  (Albano et al., 2018) and a depth of the slipping area  
428 of 3-5 km. This leads to  $\sigma = 44\text{-}124$  MPa. For  $k = G/h$  with  $G = 30$  GPa (the shear modulus near  
429 the surface) and  $h = 8$  km (rate-strengthening depth based on the coseismic slip models), we  
430 obtain  $(a-b) = 3 \times 10^{-3} - 7.8 \times 10^{-4}$ . More complex models (e.g. finite element model,  
431 heterogeneous  $(a-b)$  values) could be performed by future studies in order to reproduce the  
432 surface displacements and to propose a more precise value of  $(a-b)$ . However, our estimation  
433 is in agreement with experiments on carbonates. Scuderi and Collettini (2016) found values of  
434  $(a - b)$  evolve from velocity strengthening behaviour ( $a - b \approx 0.005$ ) at fluid pressure condition  
435 of sub-hydrostatic to a velocity neutral behaviour ( $a - b$  approaching 0), when the fault is at  
436 near lithostatic fluid pressure. Pluymakers et al., (2016) found that wet anhydrite and dolomite  
437 gouges at depths  $< 6$  km, exhibit  $(a-b)$  values ranging from  $10^{-2}$  to  $10^{-4}$ .

438 In Arquata del Tronto, the obtained (a-b) positive value (0.0026) is in agreement with  
439 a velocity-strengthening area. The obtained (a-b) value is also very low and corresponds to a  
440 quasi-neutral rate-dependency of friction implying a high sensitivity to stress perturbations.  
441 Potential stress perturbations needed to reach strengthening may involve either a decrease in  
442 effective normal stress and / or an increase in shear stress (Scholz, 1998). Walters et al., (2018)  
443 calculated the Coulomb stress change (CFF) after the Norcia earthquake. At shallow depths,  
444 they found a positive CFF change below Arquata del Tronto, which might have triggered the  
445 observed afterslip in this area. An increase in pore fluid pressure would have a similar effect.  
446 The afterslip is located near to the Olevano-Antrodoco-Sibillini (OAS) thrust. Chiarabba et al.,  
447 (2018) detected a high  $V_p/V_s$  near the OAS thrust (around 3 km depth), indicating high pore  
448 pressure that could have been further increased by nearby major shocks (Amatrice and Norcia  
449 earthquake). This high pore pressure could have induced the observed afterslip allowing for  
450 the release of the residual accumulated stress. This scenario is also supported by the fact that  
451 pore fluid pressure variation is common in this area, where the inherited structures seem to  
452 control the rupture pattern and could also concentrate high shear stress. Future work could  
453 examine detailed Coulomb Stress modelling with high spatial resolution taking all fault  
454 complexity and pore fluid effects into account. These works could be useful, despite some  
455 limitations related to the resolution of the coseismic slip and by the ambiguity about which  
456 faults were involved.

457 If this overlapping of coseismic slip and afterslip is real below 4-5 km depth (below  
458 Arquata del Tronto) could be an artefact caused by the smoothing used to regularize the  
459 inversion of the slip distribution, combined with the fact that the resolution at depth is limited.  
460 If this overlapping of co-seismic and slow slip was confirmed, a simple interpretation of rate  
461 and state friction cannot be proposed here. Overlaps between coseismic slip and afterslip have  
462 been observed after several earthquakes. For example after 2004  $M_w$  6 Parkfield earthquake,  
463 afterslip was inferred to overlap the coseismic slip (Freed, 2007). Johnson et al., (2006)  
464 proposed frictional spatial heterogeneity to explain the afterslip distribution, and proposed (a-  
465 b) values on the order of  $10^{-4} - 10^{-3}$ . After the 2015 Ilael  $M_w$  8 megathrust earthquake,  
466 Barnhart et al. (2016) also observed afterslip and coseismic slip overlapping, and advocated  
467 that stress heterogeneities likely provide the primary control on the afterslip distribution. After  
468 the 1978  $M_w$  7.3 Tabas-e-Golshan earthquake, Zhou et al., (2018) also observe such  
469 overlapping and found  $(a-b) \sim 3 \cdot 10^{-3}$ . They proposed that the fault is creeping during the whole

470 interseismic period and that the earthquake propagates through the rate-strengthening region  
471 although they also stated that a change in frictional properties is also possible due to shear  
472 heating. Thomas et al., (2017), after the 2003  $M_w$  6.8 Chengkung earthquake estimated that  
473 (a-b) varies with depth from 0.018 near the surface to less than 0.001 at depth larger than 19  
474 km, to explain areas showing both seismic and aseismic behavior they advocated shear heating  
475 processes. Using numerical modelling, Noda and Lapusta (2013) argued that coseismic slip  
476 could propagate into velocity-strengthening regions of a fault, and that these regions can  
477 appear locked or creeping during the interseismic period. They observed this behavior due to  
478 rapid shear heating. For our case it is difficult to pinpoint the particular fault zone mechanism  
479 here, but we can propose a switch to (a-b) positive value below 4-5 km depth, due to coseismic  
480 shear heating processes (Thomas et al., 2017) requiring temperature changes of several  
481 hundred degrees (e.g., Rice, 2006). This could be a potential explanation since Smeraglia et al.,  
482 (2017) suggested that nanostructures from the Mt Vettoreto Fault rocks were generated by  
483 coseismic shear heating and grain comminution (reduction of particle sizes).

484

## 485 5.2 Barrier of rupture propagation

486 Near Arquata del Tronto, at shallow depth (< 3-4 km) we observe that the aseismic slip is  
487 localized on an area associated with limited coseismic slip, for both the Amatrice and Norcia  
488 earthquakes. The observed aseismic slip seems located in an area where coseismic ruptures  
489 have not propagated during the Norcia or Amatrice earthquakes. This slowly slipping zone is  
490 located near a structural complexity (inherited thrust OAS), that Chiaraluce et al., (2017), Pizzi  
491 et al., (2017) and Puliti et al. (2020) interpreted as a barrier that concentrated stress after the  
492 Amatrice earthquake. We propose that maybe as a result of this geometric complexity (that  
493 may concentrate high stress and high porosity resulting from fracturation), this zone might be  
494 also characterized by frictional properties at shallow depth that could have favoured the arrest  
495 of the ruptures (e.g., Kaneko et al., 2010). Scholz (1998) shows that when an earthquake  
496 propagates into a velocity strengthening field it will produce a negative stress drop, that rapidly  
497 terminates propagation. Our simple calculations yield here a slightly positive (a-b) value,  
498 consistent with this model.

## 499 6 Conclusion

500 The Sentinel-1 InSAR time-series show cm-scale post-seismic displacements after the  
501 Norcia earthquake (October 30). The displacements are more obvious in the ascending track  
502 than in the descending track, and correspond to ~1 to 5 cm of subsidence in the Castelluccio  
503 basin and at the southern tip of the Norcia surface rupture. In the area of the Castelluccio  
504 basin, whether the deformation can be explained by afterslip only is less clear and would  
505 require additional modelling to include the effects of poro-elastic release or shear zone  
506 deformation. At the southern edge of the Norcia coseismic rupture, deformation evolves with  
507 time following a logarithmic decay consistent with afterslip triggered by the Norcia  
508 earthquake. Although good observations of the 2.6 first days of afterslip are not available, after  
509 3 months the slow deformation evidenced in this study released a geodetic moment of Mw  
510 ~5.78, which corresponds to ~8.7 % of the geodetic moment released during the Norcia  
511 earthquake. Cumulated moment released by aftershocks in the southern tip of the Norcia  
512 rupture accounts for ~2.0 % of the moment released by the modelled deformation, the  
513 deformation is thus here mainly aseismic. This afterslip takes place at the southern tip of the  
514 Norcia rupturing patch, and seems to have acted as a barrier to the propagation of Norcia and  
515 Amatrice ruptures at shallow depth (<3-4 km). Our results suggest that the observed post-  
516 Norcia earthquake afterslip might have been triggered in response to heterogeneities of pore  
517 fluid pressure, potentially facilitated by structural complexity and intense faulting in the area.  
518 Such small and localized slow deformation due to afterslip may be best detected with InSAR  
519 time-series in regions of sparse GNSS coverage. It might actually be quite common and could  
520 be an underestimated phenomenon. This likely points toward a bias in the literature in favour  
521 of high and wider afterslip, that is easier to detect. However detection of small afterslip  
522 transient is crucial to further understand the physics of earthquakes, and the link between  
523 slow slip and seismic rupture (e.g., Kaneko et al., 2010; Rousset et al., 2017).

524

525 7 Tables

526

527 7.1 Table 1

528

	Depths (km)	Model 1 $\eta$	Model 2 $\eta$	Model 3 $\eta$	Model 4 $\eta$
<b>Upper crust</b>	0-10.7	Elastic	Elastic	Elastic	Elastic
<b>Middle crust</b>	10.7-21.7	Elastic	$10^{19}$ Pa s	$10^{18}$ Pa s	$10^{18}$ Pa s
<b>Lower crust</b>	21.7-33.1	$10^{18}$ Pa s	$10^{18}$ Pa s	$10^{18}$ Pa s	$10^{17}$ Pa s
<b>Upper mantle</b>	33.1-below	$10^{21}$ Pa s	$10^{21}$ Pa s	$10^{21}$ Pa s	$10^{21}$ Pa s

529

530 Table 1 : Crust and mantle viscosities ( $\eta$ ) tested in Figure 6.

531

532

533 7.2 Table 2

534

Fit	$\alpha$	C (days <sup>-1</sup> )	$\gamma$	R2
<b>Point 1 near Arquata del Tronto</b>	$30.9 \pm 4.0$	$0.26 \pm 0.26$	$-6.4 \pm 6.2$	0.87
<b>Point 2 near Castelluccio di Norcia</b>	$156.4 \pm 230.7$	$0.003 \pm 0.007$	$2.54 \pm 3.5$	0.81
<b>Pattern tracking</b>	$1.6 \pm 0.1$	$0.24 \pm 0.1$	$-0.37 \pm 0.21$	0.95

535

536 Table 2: Parameters obtained from the fit of the afterslip model in Figure 3 using a non-linear

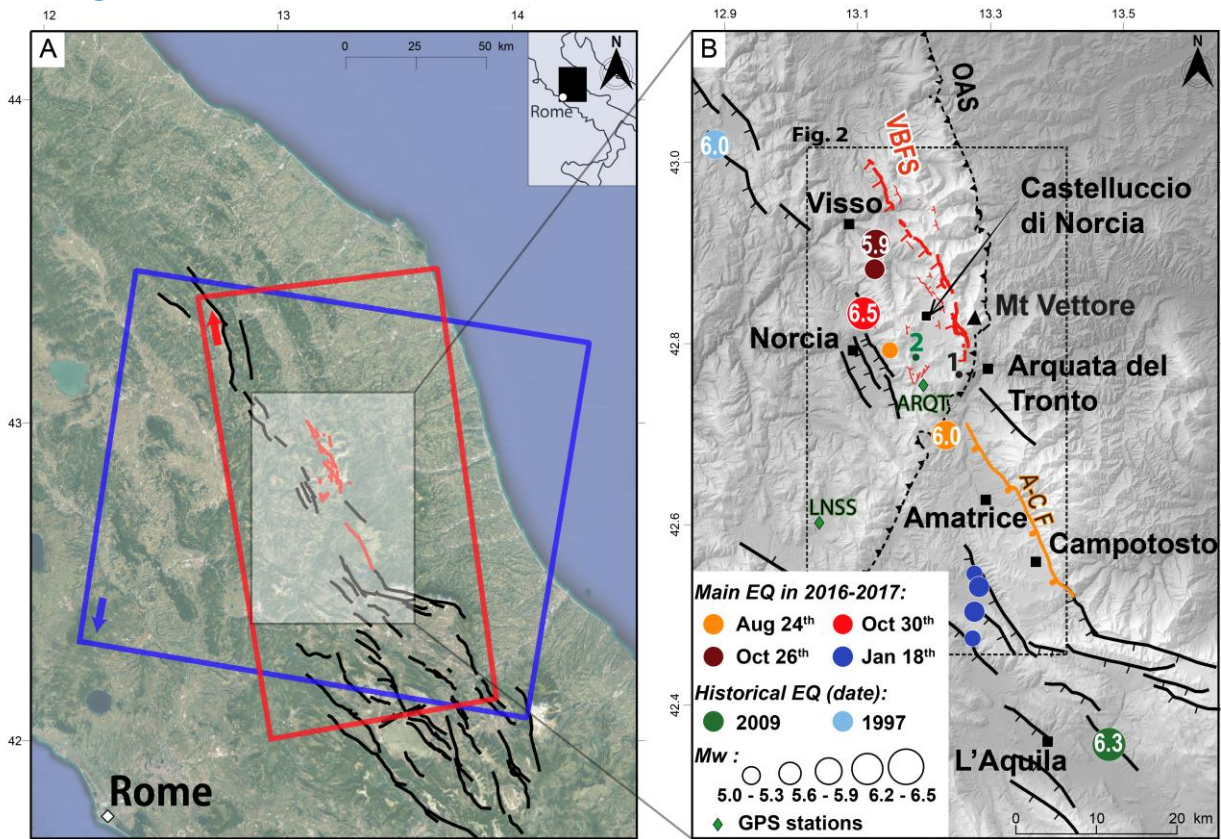
537 least squares method (Moré, 1978). R2 is the coefficient of determination of the regression.

538 The pattern encompasses the point 1 (see Figure 4)

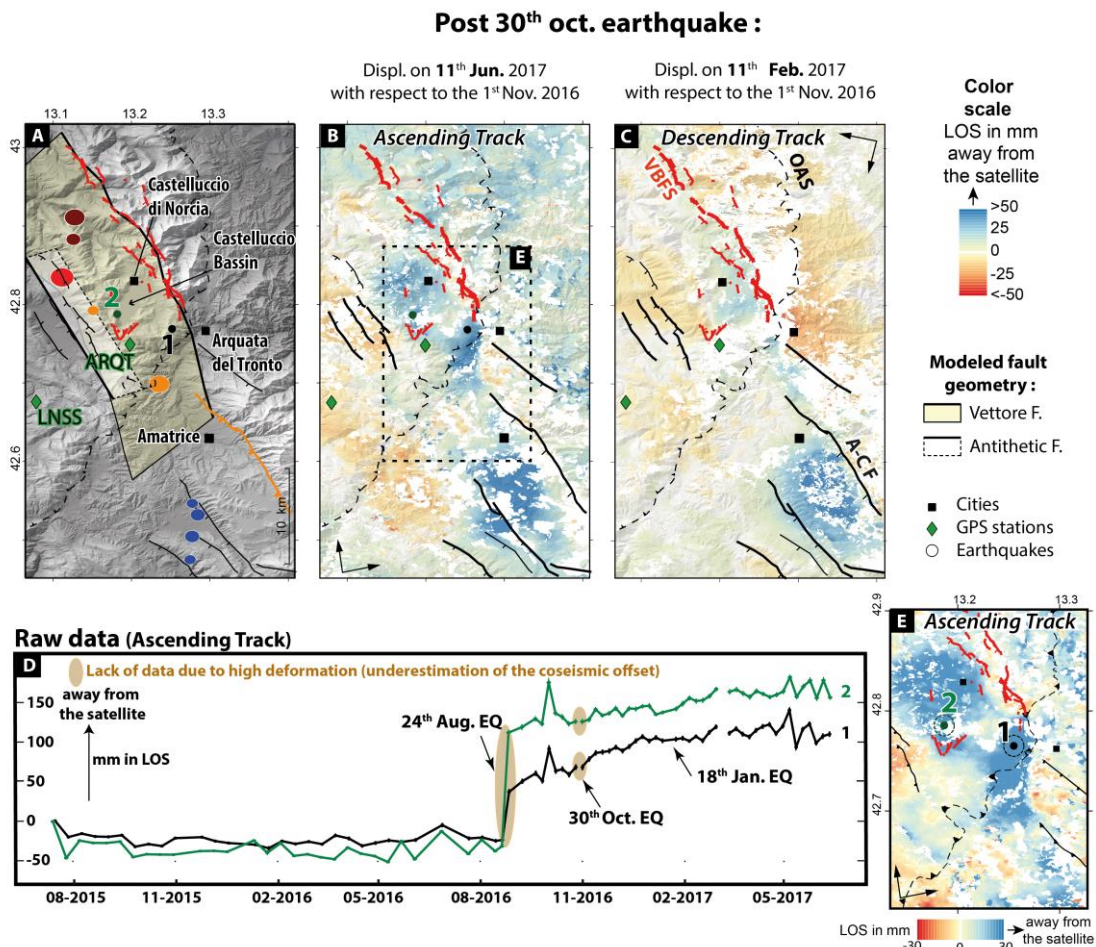
539

540 8 Figures

541 8.1 Figure 1

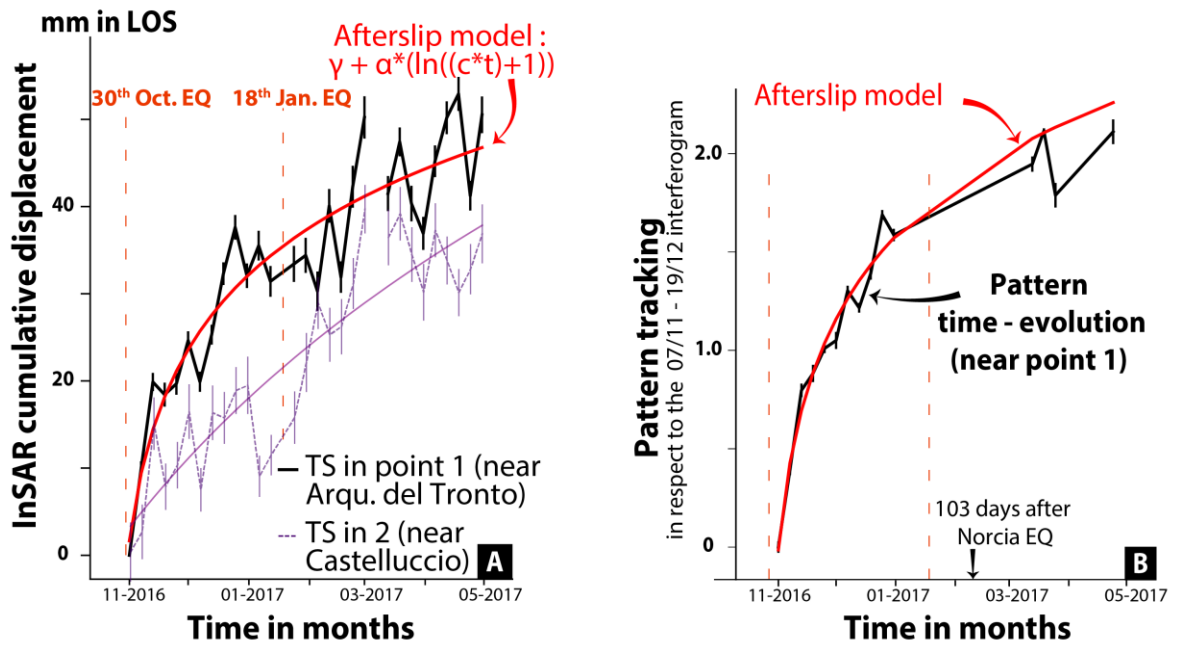


542  
 543 Figure 1: Neotectonic framework of the Central Apennines. Black lines are main normal active  
 544 faults compiled from Benedetti (1999), Tesson et al., (2016) and references therein (VBFS: Mt  
 545 Vettore – Mt Bove Fault System, A-C F: Amatrice-Campotosto Fault). In red, coseismic surface  
 546 ruptures observed in the field after the mainshocks of the Central Italy 2016-2017 seismic  
 547 sequence (Villani, Civico, et al., 2018). **(A)** Blue and red rectangles are, respectively, the  
 548 descending (D22 subswaths IW2 and IW3) and ascending (A117, subswath IW3) Sentinel tracks  
 549 processed in this study. **(B)** Black dashed line represents the Neogene OAS thrust (Olevano-  
 550 Antrodoco-Sibillini thrust) (Di Domenica et al., 2012). In orange the Amatrice-Campotosto fault  
 551 which was activated during the 2016—2017 seismic sequence. ARQT and LNSS (in B) are GNSS  
 552 stations available in this region from  
 553 [http://geodesy.unr.edu/NGLStationPages/gpsnetmap/GPSNetMap\\_MAG.html](http://geodesy.unr.edu/NGLStationPages/gpsnetmap/GPSNetMap_MAG.html) (Blewitt et al.,  
 554 2018).  
 555



557  
 558 Figure 2: (A) Map of the studied area, green squares are the GPS stations, points 1-2 are the  
 559 points of sampling. The modeled geometries of the Mt Vettore and antithetic faults are plotted  
 560 (see section 4.5). Circles are the earthquakes (see Figure 1). **(B-C)**: Time-series calculated  
 561 cumulative post-Norcia (30 oct) displacements for ascending (B) and descending track (C),  
 562 respectively. In panels A,B,C,E : Red lines are surface ruptures associated with 30<sup>th</sup> October  
 563 2016 Norcia earthquake (Villani, Civico, et al., 2018), and black lines are active faults. Black  
 564 dashed line is the OAS thrust. (VBFS: Mt Vettore – Mt Bove Fault System, A-C F: Amatrice-  
 565 Campotosto Fault, OAS: Olevano-Anrodoco-Sibillini thrust). **(D)** Displacement through time  
 566 averaged over a circle of 20 pixels (dashed circles in panel E) in diameter around points 1-2. **(E)**  
 567 Cumulative displacement on June 11, 2017, with respect to the 1<sup>st</sup> November 2016 date.  
 568

570



571

572

573 Figure 3: **(A)** Temporal variation of displacement averaged over a circle of 20 pixels in diameter  
 574 through time of point 1 (black curve) and 2 (purple dashed curve) localized in Figure 2-E. We  
 575 fitted the curve with afterslip model (see results in Table 2).

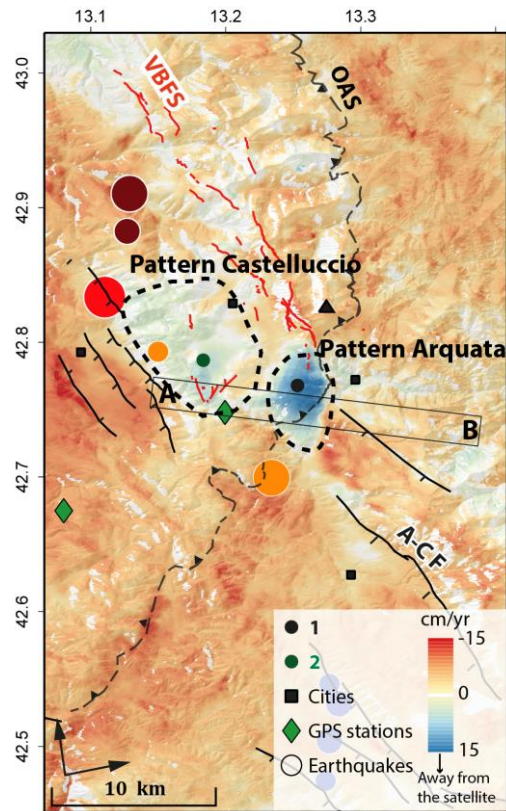
576 **(B)** Temporal variation of pattern amplitude. Pattern is indicated in Figure 4. In red, the fit with  
 577 an afterslip model (see results in Table 2).

578

579

580

581 8.4 Figure 4

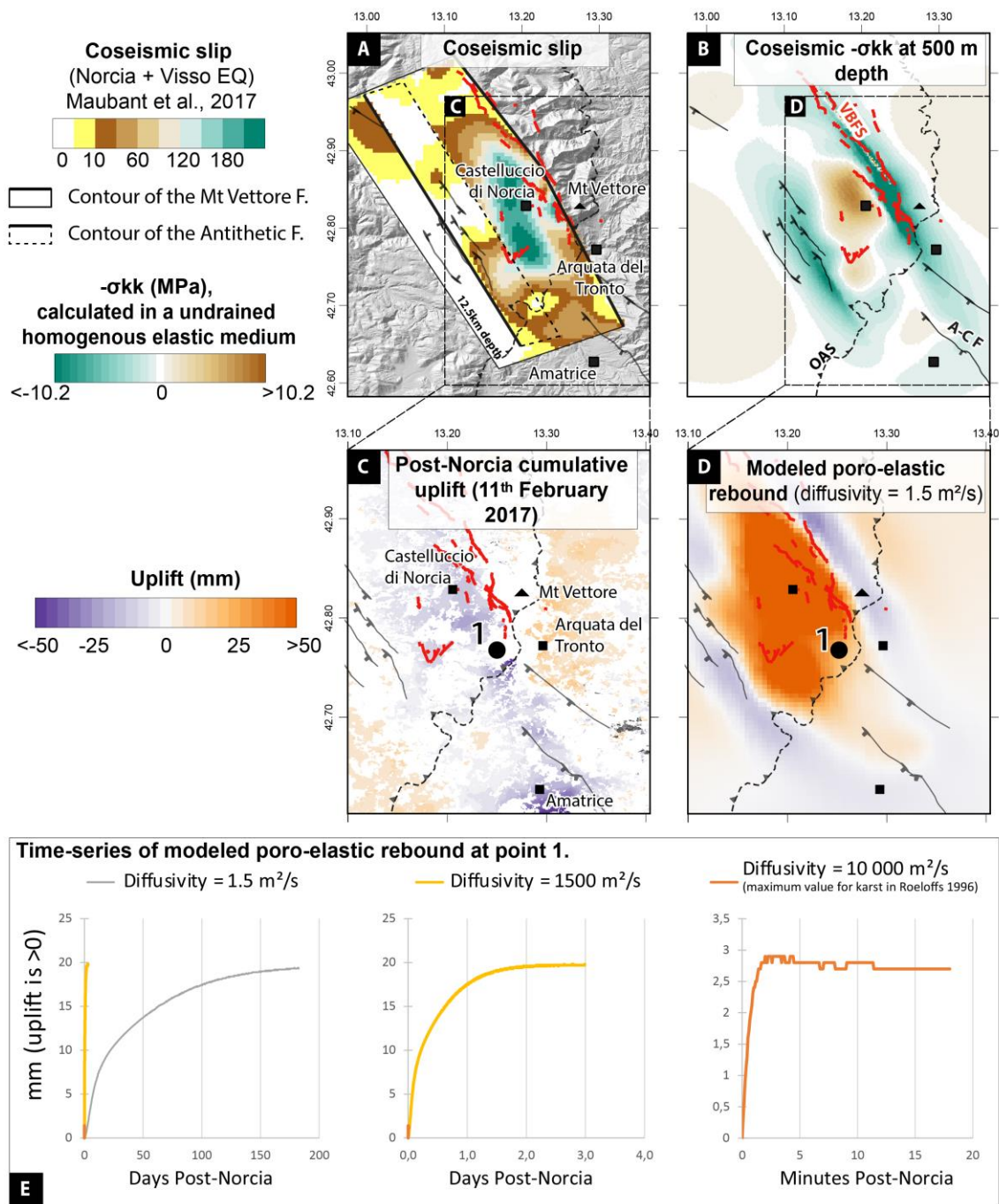


582

583 Figure 4: Mean velocity map between Mw 6.5 Norcia and Mw 5.7 Campotosto earthquakes  
584 (November 1<sup>st</sup> – January 12<sup>th</sup>). This map is computed using 35 ascending interferograms. The  
585 swath A-B is used in Figure S11 to compare InSAR displacements and topography. Circles  
586 represent the earthquakes (see color code in Figure 1).

587

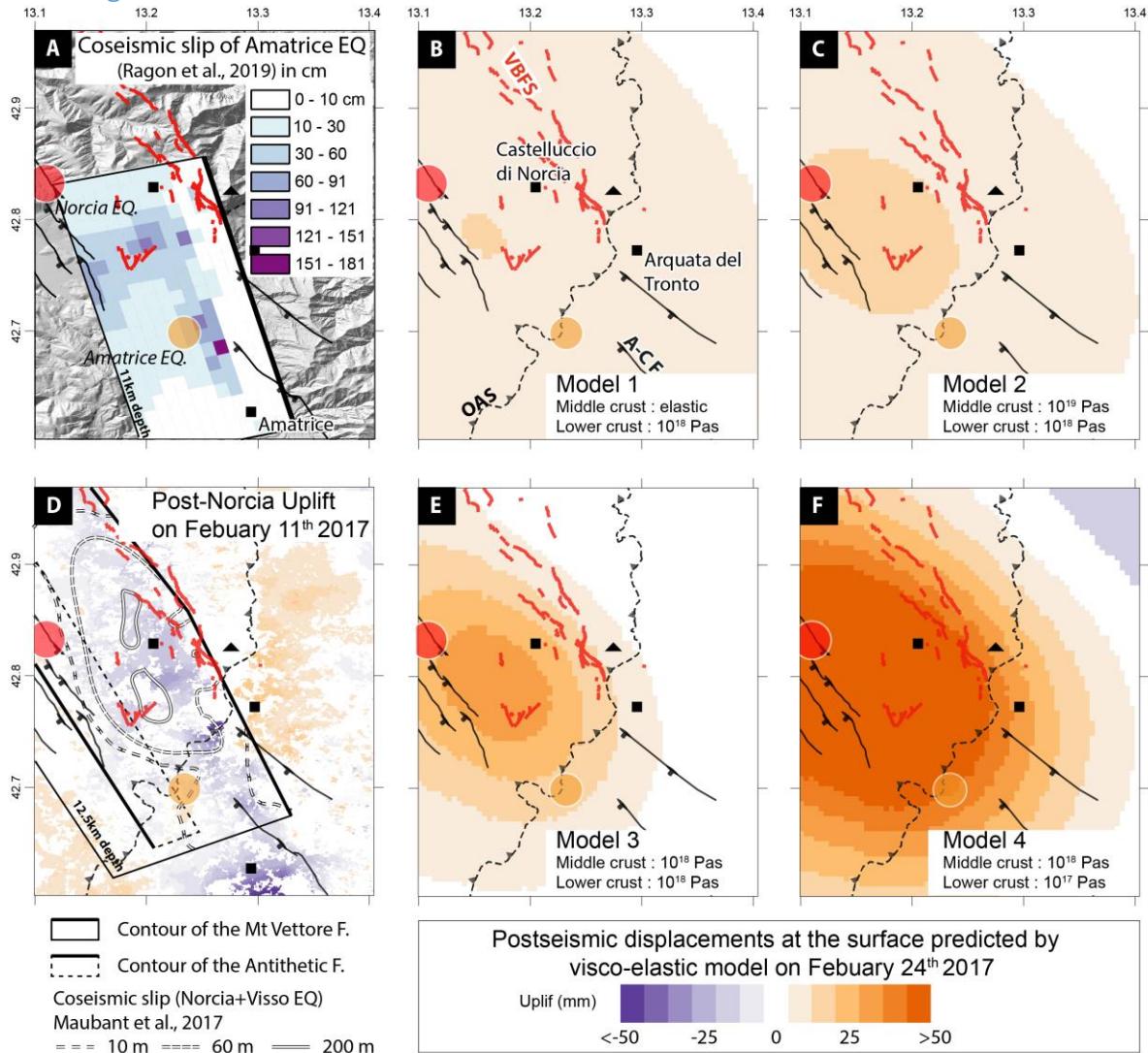
588



590

591 Figure 5: Poro-elastic rebound modelled with Relax software (Barbot & Fialko, 2010). We used  
 592 the coseismic slip models of the Norcia and Visso earthquakes from Maubant et al., (2017).  
 593 **(A)** Mapview of the coseismic slip distribution. **(B)** Coseismic  $-\sigma_{kk}$  modelled at 500m depth,  
 594 calculated in an undrained homogenous elastic medium (Poisson  $\nu=0.34$ ; Lamé  $\lambda=6.36E+04$   
 595 MPa, shear modulus  $G=30$  GPa, Gravity wavelength  $\gamma=5.39E-04$  km<sup>-1</sup>). To remind, the pore  
 596 pressure change ( $\Delta p$ ) is equal to  $-B \cdot \sigma_{kk} / 3$ , with (B the Skempton's coefficient). **(C)** Post-Norcia  
 597 cumulative displacement map (11<sup>th</sup> February 2017) observed by InSAR (uplift component). **(D)**

598 Model-predicted poro-elastic rebound as of 25<sup>th</sup> February 2017, obtained using the difference  
599 between drained and undrained conditions. Poisson drained is 0.26 (cf. layer 1 in Albano et al.  
600 2018), and for undrained conditions is 0.34 (from  $\beta=0.4$  in the table 1 and equation 15 in  
601 Barbot et al., (2010)). The layer between (0 and 5 km) is characterized by a diffusivity equals  
602 to  $1.5 \text{ m}^2/\text{s}$  (Tung & Masterlark, 2018). **(E)** Modelled poro-elastic rebound time-series at point  
603 A using several diffusivities, from  $1.5 \text{ m}^2/\text{s}$  (Tung & Masterlark, 2018) to  $10^4 \text{ m}^2/\text{s}$  (Roeloffs,  
604 1996). Because the delay time is inversely proportional to the assumed diffusivity, the  
605 response for high diffusivity is shorter. (VBFS: Mt Vettore – Mt Bove Fault System, A-C F:  
606 Amatrice-Campotosto Fault, OAS: Olevano-Antrodoco-Sibillini thrust).  
607

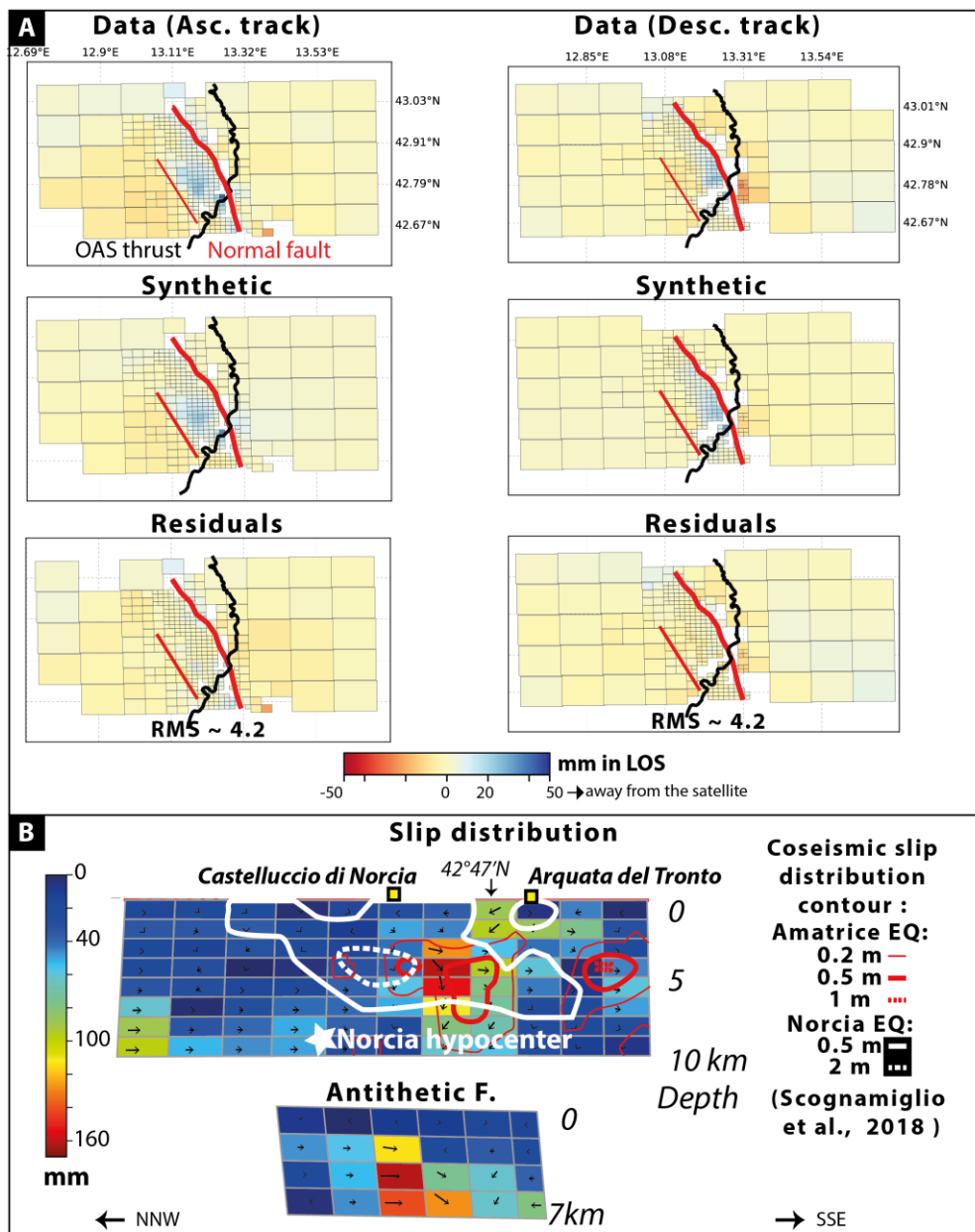


609

610 Figure 6: Surface displacements predicted by visco-elastic models, we used the Amatrice,  
 611 Norcia and Visso earthquakes coseismic slip distribution modelled by Ragon et al., (2019) and  
 612 Maubant et al., (2017). **(A)** Coseismic slip distribution of the Amatrice earthquake from Ragon  
 613 et al., (2019) **(B-C-E-F)** Surface displacements predicted by four visco-elastic models on 24<sup>th</sup>  
 614 February 2017 using Relax software (Barbot & Fialko, 2010). Mantle viscosity is fixed for all  
 615 models at  $10^{21}$  Pas. **(D)** Post-Norcia earthquake (30<sup>th</sup> October) cumulative displacement map  
 616 (11<sup>th</sup> February 2017) observed by InSAR (uplift component). (VBFS: Mt Vettore – Mt Bove Fault  
 617 System, A-C F: Amatrice-Campotosto Fault, OAS: Olevano-Antrodoco-Sibillini thrust)

618

619

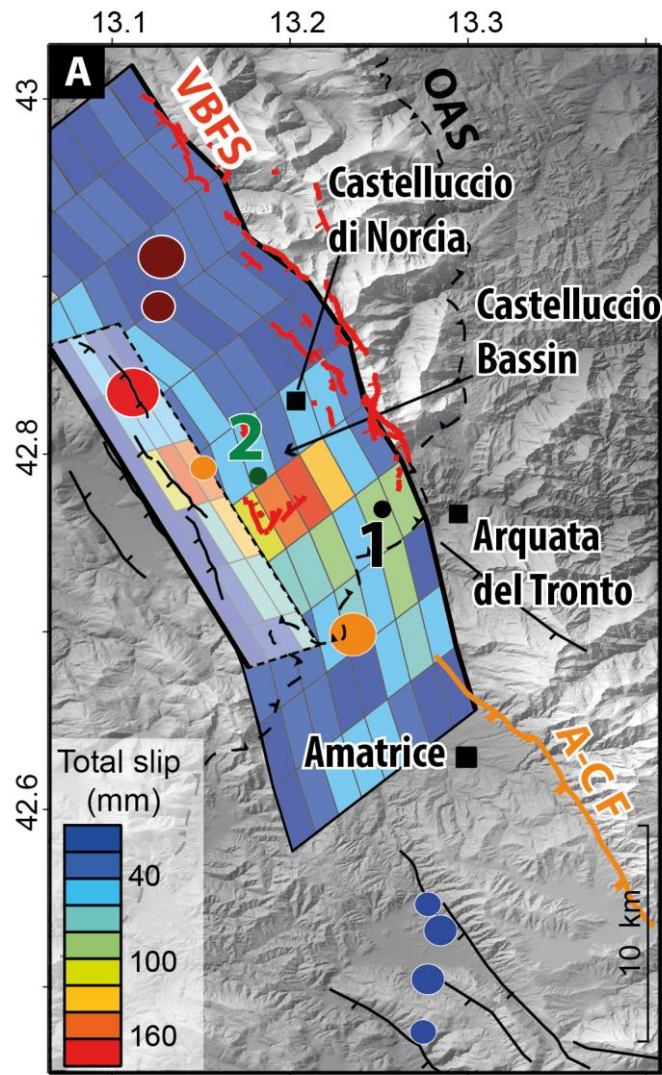


622  
623 Figure 7: Result of afterslip inversion using the CSI software (see Supplementary text S3 for  
624 details). **(A)** Subsampled displacement maps for the ascending (left column) and descending  
625 (right column) tracks. Top row shows the input subsampled data, middle row shows the  
626 synthetic displacements predicted by the model, and bottom row shows the residuals (i.e.  
627 model - data). The modeled fault geometries used for the inversion are plotted in Figure 2-A.  
628 The input maps are the smoothed cumulative displacement maps on February 11<sup>th</sup> (calculated  
629 in the ascending and descending post-30<sup>th</sup> October time-series). **(B)** Afterslip distribution  
630 inverted from the data on the main fault and the antithetic fault. Black arrows in patches show  
631 the rake. Our model has low resolution at depth (Figure S16). Coseismic slip distributions for

632 the Amatrice and Norcia earthquakes (Scognamiglio et al., (2018) are superimposed in white  
633 and red , respectively. Comparison with the Cheloni et al.,(2019) model in Figure S21 shows  
634 similar patterns.

635

636



638  
 639 Figure 8: Afterslip distribution model plotted on mapview. The slip distribution is inverted from  
 640 the data on the main fault and the antithetic fault (see Figure 7). (VBFS: Mt Vettore – Mt Bove  
 641 Fault System, A-C F: Amatrice-Campotosto Fault). Circles are the main earthquakes of the  
 642 seismic sequence.  
 643

## 644 9 Acknowledgments

645 We would like to thank the Editor, Associate Editor, Mong-Han Huang and two anonymous  
646 reviewers for their constructive suggestions, which helped to improve the manuscript substantially. We  
647 acknowledge the French Spatial Agency CNES (Centre National d'Etudes Spatiales) for funding this  
648 study (Program THEIA and CNES post-doctorate fellowship for L.Pousse-Beltran). This work was also  
649 funded through the TELLUS-ALEAS program from Institut des Sciences de l'Univers (INSU). CNES is  
650 warmly acknowledged from providing us with the Pléiades satellite images through ISIS and  
651 CEOS\_seismic pilot (ESA) programs. Nicola D'Agostino was under an invited researcher position at Univ.  
652 Grenoble Alpes - OSUG - ISTERre when most of the work was performed. Most of the computations  
653 presented in this paper were performed using the Luke platform of the CIMENT infrastructure  
654 (<https://ciment.ujf-grenoble.fr>), which is supported by the Rhône-Alpes region (grant CPER07\_13  
655 CIRA), the OSUG@2020 labex (reference ANR10 LABX56), and the Equip@Meso project (reference  
656 ANR-10-EQPX-29-01) of the programme Investissements d'Avenir supervised by the Agence Nationale  
657 pour la Recherche. Franck Thollard, Christophe Laurent, Erwan Pathier, Louise Maubant and Simon  
658 Daout are warmly acknowledged for help and advice on NSBAS processing chain. We are also grateful  
659 to Théa Ragon and Romain Jolivet for support and advice in slip distribution modelling, the CSI software  
660 will be soon released online. We thank Louise Maubant and James Hollingsworth for sharing the Norcia  
661 slip distribution model. Alberto Pizzi, Bruno Pace, Paolo Boncio and Irene Puliti are also warmly  
662 acknowledged for fruitful discussions. The European Space Agency (ESA) Copernicus program has  
663 provided free and high-quality SAR data from Sentinel-1A and 1B (ESA,  
664 <https://scihub.copernicus.eu>) through the PEPS platform of CNES (Copernicus 2018 for Sentinel  
665 data. We thank Simone Tarquini for the supply of 10 m resolution TINITALY DEM. The afterslip  
666 distribution model will be provided in [10.5281/zenodo.3755127](https://doi.org/10.5281/zenodo.3755127) . Seismicity used for this research is  
667 included in (Chiaraluce et al., 2017) and in <http://cnt.rm.ingv.it/>. The GNSS stations are downloaded  
668 from <http://geodesy.unr.edu/NGLStationPages/stations/>

669

## 670 10 References

671

- 672 Albano, M., Barba, S., Solaro, G., Pepe, A., Christian, B., Moro, M., et al. (2017). Aftershocks,  
673 groundwater changes and postseismic ground displacements related to pore pressure  
674 gradients: Insights from the 2012 Emilia-Romagna earthquake. *Journal of Geophysical*  
675 *Research: Solid Earth*, 122(7), 5622–5638. <https://doi.org/10.1002/2017JB014009>
- 676 Albano, M., Barba, S., Saroli, M., Polcari, M., Bignami, C., Moro, M., et al. (2018). Aftershock  
677 rate and pore fluid diffusion: Insights from the Amatrice-Visso-Norcia (Italy) 2016  
678 seismic sequence. *Journal of Geophysical Research: Solid Earth*, 0(ja).  
679 <https://doi.org/10.1029/2018JB015677>
- 680 Amoruso, A., Crescentini, L., D’Anastasio, E., & Martini, P. M. D. (2005). Clues of postseismic  
681 relaxation for the 1915 Fucino earthquake (central Italy) from modeling of leveling  
682 data. *Geophysical Research Letters*, 32(22). <https://doi.org/10.1029/2005GL024139>
- 683 Aoudia, A., Borghi, A., Riva, R., Barzaghi, R., Ambrosius, B. a. C., Sabadini, R., et al. (2003).  
684 Postseismic deformation following the 1997 Umbria-Marche (Italy) moderate normal  
685 faulting earthquakes. *Geophysical Research Letters*, 30(7).  
686 <https://doi.org/10.1029/2002GL016339>
- 687 Aslan, G., Lasserre, C., Cakir, Z., Ergintav, S., Özarpaci, S., Dogan, U., et al. (2019). Shallow Creep  
688 Along the 1999 Izmit Earthquake Rupture (Turkey) From GPS and High Temporal  
689 Resolution Interferometric Synthetic Aperture Radar Data (2011–2017). *Journal of*  
690 *Geophysical Research: Solid Earth*, 124(2), 2218–2236.  
691 <https://doi.org/10.1029/2018JB017022>
- 692 Avouac, J.-P. (2015). From Geodetic Imaging of Seismic and Aseismic Fault Slip to Dynamic  
693 Modeling of the Seismic Cycle. *Annual Review of Earth and Planetary Sciences*, 43(1),  
694 233–271. <https://doi.org/10.1146/annurev-earth-060614-105302>
- 695 Barbot, S., & Fialko, Y. (2010). A unified continuum representation of post-seismic relaxation  
696 mechanisms: semi-analytic models of afterslip, poroelastic rebound and viscoelastic  
697 flow: Semi-analytic models of postseismic transient. *Geophysical Journal International*,  
698 182(3), 1124–1140. <https://doi.org/10.1111/j.1365-246X.2010.04678.x>

699 Barnhart, W. D., Murray, J. R., Briggs, R. W., Gomez, F., Miles, C. P. J., Svarc, J., et al. (2016).  
700 Coseismic slip and early afterslip of the 2015 Illapel, Chile, earthquake: Implications for  
701 frictional heterogeneity and coastal uplift. *Journal of Geophysical Research: Solid Earth*,  
702 *121*(8), 6172–6191. <https://doi.org/10.1002/2016JB013124>

703 Benedetti, L. (1999). *Sismotectonique de l'Italie et des régions adjacentes: fragmentation du*  
704 *promontoire adriatique* (PhD Thesis). Paris 7.

705 Blewitt, G., Hammond, W., & Kreemer, C. (2018). Harnessing the GPS Data Explosion for  
706 Interdisciplinary Science. *Eos*, *99*. <https://doi.org/10.1029/2018EO104623>

707 Boni, C. F., TARRAGONI, C., MARTARELLI, L., & PIERDOMINICI, S. (2010). STUDIO  
708 IDROGEOLOGICO NEL SETTORE NORD-OCCIDENTALE DEI MONTI SIBILLINI: UN  
709 CONTRIBUTO ALLA CARTOGRAFIA IDROGEOLOGICA UFFICIALE. *Italian Journal of*  
710 *Engineering Geology and Environment*, *2*, 16. <https://doi.org/10.4408/IJEGE.2010->  
711 [02.O-02](https://doi.org/10.4408/IJEGE.2010-02.O-02)

712 Brozzetti, F., Boncio, P., Cirillo, D., Ferrarini, F., Nardis, R. de, Testa, A., et al. (2019). High-  
713 Resolution Field Mapping and Analysis of the August–October 2016 Coseismic Surface  
714 Faulting (Central Italy Earthquakes): Slip Distribution, Parameterization, and  
715 Comparison With Global Earthquakes. *Tectonics*, *0*(0).  
716 <https://doi.org/10.1029/2018TC005305>

717 Bürgmann, R. (2018). The geophysics, geology and mechanics of slow fault slip. *Earth and*  
718 *Planetary Science Letters*, *495*, 112–134. <https://doi.org/10.1016/j.epsl.2018.04.062>

719 Calamita, F., Cello, G., Deiana, G., & Paltrinieri, W. (1994). Structural styles, chronology rates of  
720 deformation, and time-space relationships in the Umbria-Marche thrust system  
721 (central Apennines, Italy). *Tectonics*, *13*(4), 873–881.  
722 <https://doi.org/10.1029/94TC00276>

723 Calamita, F., Satolli, S., Scisciani, V., Eserstine, P., & Pace, P. (2011). Contrasting styles of fault  
724 reactivation in curved orogenic belts: Examples from the Central Apennines (Italy).  
725 *Geological Society of America Bulletin*, *123*(5–6), 1097–1111.  
726 <https://doi.org/10.1130/B30276.1>

- 727 Calamita, F., Satolli, S., & Turtù, A. (2012). Analysis of thrust shear zones in curve-shaped belts:  
728 Deformation mode and timing of the Olevano-AnTRODoco-Sibillini thrust  
729 (Central/Northern Apennines of Italy). *Journal of Structural Geology*, *44*, 179–187.  
730 <https://doi.org/10.1016/j.jsg.2012.07.007>
- 731 Carafa, M. M. C., & Bird, P. (2016). Improving deformation models by discounting transient  
732 signals in geodetic data: 2. Geodetic data, stress directions, and long-term strain rates  
733 in Italy. *Journal of Geophysical Research: Solid Earth*, *121*(7), 5557–5575.  
734 <https://doi.org/10.1002/2016JB013038>
- 735 Cavalié, O., Doin, M.-P., Lasserre, C., & Briole, P. (2007). Ground motion measurement in the  
736 Lake Mead area, Nevada, by differential synthetic aperture radar interferometry time  
737 series analysis: Probing the lithosphere rheological structure. *Journal of Geophysical*  
738 *Research: Solid Earth*, *112*(B3), n/a–n/a. <https://doi.org/10.1029/2006JB004344>
- 739 Cheloni, D., De Novellis, V., Albano, M., Antonioli, A., Anzidei, M., Atzori, S., et al. (2017).  
740 Geodetic model of the 2016 Central Italy earthquake sequence inferred from InSAR  
741 and GPS data. *Geophysical Research Letters*, *44*(13), 2017GL073580.  
742 <https://doi.org/10.1002/2017GL073580>
- 743 Cheloni, D., Falcucci, E., & Gori, S. (2019). Half-graben rupture geometry of the 30 October  
744 2016 MW 6.6 Mt. Vettore-Mt. Bove earthquake, central Italy. *Journal of Geophysical*  
745 *Research: Solid Earth*, *0*(ja). <https://doi.org/10.1029/2018JB015851>
- 746 Chen, K. H., & Bürgmann, R. (2017). Creeping faults: Good news, bad news? *Reviews of*  
747 *Geophysics*, *55*(2), 2017RG000565. <https://doi.org/10.1002/2017RG000565>
- 748 Chiarabba, C., Gori, P. D., Cattaneo, M., Spallarossa, D., & Segou, M. (2018). Faults geometry  
749 and the role of fluids in the 2016-2017 Central Italy seismic sequence. *Geophysical*  
750 *Research Letters*, *0*(ja). <https://doi.org/10.1029/2018GL077485>
- 751 Chiaraluce, L., Stefano, R. D., Tinti, E., Scognamiglio, L., Michele, M., Casarotti, E., et al. (2017).  
752 The 2016 Central Italy Seismic Sequence: A First Look at the Mainshocks, Aftershocks,  
753 and Source Models. *Seismological Research Letters*, *88*(3), 757–771.  
754 <https://doi.org/10.1785/0220160221>

755 Cirella, A., Pezzo, G., & Piatanesi, A. (2018). Rupture Kinematics and Structural - Rheological  
756 Control of the 2016 Mw6.1 Amatrice (Central Italy) Earthquake from Joint Inversion of  
757 Seismic and Geodetic Data. *Geophysical Research Letters*, *0*(ja).  
758 <https://doi.org/10.1029/2018GL080894>

759 Civico, R., Pucci, S., Villani, F., Pizzimenti, L., Martini, P. M. D., Nappi, R., & Group, the O. E.  
760 W. (2018). Surface ruptures following the 30 October 2016 Mw 6.5 Norcia earthquake,  
761 central Italy. *Journal of Maps*, *14*(2), 151–160.  
762 <https://doi.org/10.1080/17445647.2018.1441756>

763 D’Agostino, N. (2014). Complete seismic release of tectonic strain and earthquake recurrence  
764 in the Apennines (Italy). *Geophysical Research Letters*, *41*(4), 1155–1162.  
765 <https://doi.org/10.1002/2014GL059230>

766 D’Agostino, N., Cheloni, D., Fornaro, G., Giuliani, R., & Reale, D. (2012). Space-time distribution  
767 of afterslip following the 2009 L’Aquila earthquake. *Journal of Geophysical Research:  
768 Solid Earth*, *117*, n/a-n/a. <https://doi.org/10.1029/2011jb008523>

769 Daout, S., Jolivet, R., Lasserre, C., Doin, M.-P., Barbot, S., Tapponnier, P., et al. (2016). Along-  
770 strike variations of the partitioning of convergence across the Haiyuan fault system  
771 detected by InSAR. *Geophysical Journal International*, *205*(1), 536–547.

772 Daout, S., Sudhaus, H., Kausch, T., Steinberg, A., & Dini, B. (2019). Interseismic and Postseismic  
773 Shallow Creep of the North Qaidam Thrust Faults Detected with a Multitemporal InSAR  
774 Analysis. *Journal of Geophysical Research: Solid Earth*, *124*(7), 7259–7279.  
775 <https://doi.org/10.1029/2019JB017692>

776 Devoti, R., D’Agostino, N., Serpelloni, E., Pietrantonio, G., Riguzzi, F., Avallone, A., et al. (2017).  
777 A Combined Velocity Field of the Mediterranean Region. *Annals of Geophysics*, *60*(2).  
778 <https://doi.org/10.4401/ag-7059>

779 Di Domenica, A., Turtù, A., Satolli, S., & Calamita, F. (2012). Relationships between thrusts and  
780 normal faults in curved belts: New insight in the inversion tectonics of the Central-  
781 Northern Apennines (Italy). *Journal of Structural Geology*, *42*, 104–117.  
782 <https://doi.org/10.1016/j.jsg.2012.06.008>

783 Dieterich, J. H. (1979). Modeling of rock friction: 1. Experimental results and constitutive  
784 equations. *Journal of Geophysical Research: Solid Earth*, 84(B5), 2161–2168.  
785 <https://doi.org/10.1029/JB084iB05p02161>

786 Doin, M.-P., Lodge, F., Guillaso, S., Jolivet, R., Lasserre, C., Ducret, G., et al. (2011). Presentation  
787 of the small baseline NSBAS processing chain on a case example: the Etna deformation  
788 monitoring from 2003 to 2010 using ENVISAT data. In *Proceedings of the Fringe*  
789 *symposium, Frascati, Italy, ESA SP-697*.

790 Doin, M.-P., Twardzik, C., Ducret, G., Lasserre, C., Guillaso, S., & Jianbao, S. (2015). InSAR  
791 measurement of the deformation around Siling Co Lake: Inferences on the lower crust  
792 viscosity in central Tibet. *Journal of Geophysical Research: Solid Earth*, 120(7), 5290–  
793 5310. <https://doi.org/10.1002/2014JB011768>

794 Elliott, J. R., Jolivet, R., González, P. J., Avouac, J.-P., Hollingsworth, J., Searle, M. P., & Stevens,  
795 V. L. (2016). Himalayan megathrust geometry and relation to topography revealed by  
796 the Gorkha earthquake. *Nature Geoscience*, 9(2), 174–180.  
797 <https://doi.org/10.1038/ngeo2623>

798 Elliott, J. R., Walters, R. J., & Wright, T. J. (2016). The role of space-based observation in  
799 understanding and responding to active tectonics and earthquakes. *Nature*  
800 *Communications*, 7, 13844. <https://doi.org/10.1038/ncomms13844>

801 Falcucci, E., Gori, S., Bignami, C., Pietrantonio, G., Melini, D., Moro, M., et al. (2018). The  
802 Campotosto seismic gap in between the 2009 and 2016-2017 seismic sequences of  
803 central Italy and the role of inherited lithospheric faults in regional seismotectonic  
804 settings. *Tectonics*, 0(ja). <https://doi.org/10.1029/2017TC004844>

805 Freed, A. M. (2007). Afterslip (and only afterslip) following the 2004 Parkfield, California,  
806 earthquake. *Geophysical Research Letters*, 34(6), L06312.  
807 <https://doi.org/10.1029/2006GL029155>

808 Freed, A. M., & Bürgmann, R. (2004). Evidence of power-law flow in the Mojave desert mantle.  
809 *Nature*, 430(6999), 548–551. <https://doi.org/10.1038/nature02784>

810 Galadini, F., & Galli, P. (2000). Active Tectonics in the Central Apennines (Italy) –Input Data for  
811 Seismic Hazard Assessment. *Natural Hazards*, 22(3), 225–268.  
812 <https://doi.org/10.1023/A:1008149531980>

813 Grandin, R. (2009). *L'apport de la géodésie spatiale dans la compréhension du processus de*  
814 *rifting magmatique : l'exemple de l'épisode en cours en Afar Ethiopien (2005-2009)*.  
815 Institut de physique du globe (Paris). Retrieved from  
816 <http://www.theses.fr/2009GLOB0013>

817 Grandin, R. (2015). Interferometric Processing of SLC Sentinel-1 TOPS Data. In *FRINGE'15:*  
818 *Advances in the Science and Applications of SAR Interferometry and Sentinel-1 InSAR*  
819 *Workshop, Frascati, Italy, 23-27 March 2015*. Frascati, Italy.  
820 <https://doi.org/10.5270/Fringe2015.pp116>

821 Grandin, R., Doin, M.-P., Bollinger, L., Pinel-Puysségur, B., Ducret, G., Jolivet, R., & Sapkota, S.  
822 N. (2012). Long-term growth of the Himalaya inferred from interseismic InSAR  
823 measurement. *Geology*, 40(12), 1059–1062. <https://doi.org/10.1130/G33154.1>

824 Gualandi, A., Serpelloni, E., & Belardinelli, M. E. (2014). Space–time evolution of crustal  
825 deformation related to the Mw 6.3, 2009 L'Aquila earthquake (central Italy) from  
826 principal component analysis inversion of GPS position time-series. *Geophysical*  
827 *Journal International*, 197(1), 174–191. <https://doi.org/10.1093/gji/ggt522>

828 Harris, R. A. (2017). Large earthquakes and creeping faults. *Reviews of Geophysics*, 55(1),  
829 2016RG000539. <https://doi.org/10.1002/2016RG000539>

830 Hetland, E. A., & Zhang, G. (2014). Effect of shear zones on post-seismic deformation with  
831 application to the 1997 Mw 7.6 Manyi earthquake. *Geophysical Journal International*,  
832 198(1), 259–269. <https://doi.org/10.1093/gji/ggu127>

833 Hirose, H., Asano, Y., Obara, K., Kimura, T., Matsuzawa, T., Tanaka, S., & Maeda, T. (2010). Slow  
834 Earthquakes Linked Along Dip in the Nankai Subduction Zone. *Science*, 330(6010),  
835 1502–1502. <https://doi.org/10.1126/science.1197102>

836 Huang, M.-H., Fielding, E. J., Liang, C., Milillo, P., Bekaert, D., Dreger, D., & Salzer, J. (2017).  
837 Coseismic deformation and triggered landslides of the 2016 Mw 6.2 Amatrice

838 earthquake in Italy. *Geophysical Research Letters*.  
839 <https://doi.org/10.1002/2016GL071687>

840 Hussain, E., Wright, T. J., Walters, R. J., Bekaert, D. P. S., Lloyd, R., & Hooper, A. (2018). Constant  
841 strain accumulation rate between major earthquakes on the North Anatolian Fault.  
842 *Nature Communications*, 9(1), 1392. <https://doi.org/10.1038/s41467-018-03739-2>

843 Johnson, K. M. (2006). Frictional Properties on the San Andreas Fault near Parkfield, California,  
844 Inferred from Models of Afterslip following the 2004 Earthquake. *Bulletin of the*  
845 *Seismological Society of America*, 96(4B), S321–S338.  
846 <https://doi.org/10.1785/0120050808>

847 Jolivet, R., Simons, M., Agram, P. S., Duputel, Z., & Shen, Z.-K. (2015). Aseismic slip and  
848 seismogenic coupling along the central San Andreas Fault. *Geophysical Research*  
849 *Letters*, 42(2). <https://doi.org/10.1002/2014GL062222>

850 Kaneko, Y., Avouac, J.-P., & Lapusta, N. (2010). Towards inferring earthquake patterns from  
851 geodetic observations of interseismic coupling. *Nature Geoscience*, 3(5), 363–369.  
852 <https://doi.org/10.1038/ngeo843>

853 King. (1986). Speculations on the geometry of the initiation and termination processes of  
854 earthquake rupture and its relation to morphology and geological structure. *Pure and*  
855 *Applied Geophysics*, 124, 19. <https://doi.org/10.1007/BF00877216>

856 King, & Nabelek. (1985). Role of Fault Bends in the Initiation and Termination of Earthquake  
857 Rupture. *Science*, 228(4702), 984–987. <https://doi.org/10.1126/science.228.4702.984>

858 Laske, G., Masters, G., Ma, Z., & Pasyanos, M. (2013). Update on CRUST1.0 - A 1-degree Global  
859 Model of Earth's Crust, 15, EGU2013-2658. Presented at the EGU General Assembly  
860 Conference Abstracts.

861 Liu, C., Zheng, Y., Xie, Z., & Xiong, X. (2017). Rupture features of the 2016 Mw 6.2 Norcia  
862 earthquake and its possible relationship with strong seismic hazards. *Geophysical*  
863 *Research Letters*, 44(3), 1320–1328. <https://doi.org/10.1002/2016GL071958>

864 López-Quiroz, P., Doin, M.-P., Tupin, F., Briole, P., & Nicolas, J.-M. (2009). Time series analysis of  
865 Mexico City subsidence constrained by radar interferometry. *Journal of Applied*  
866 *Geophysics*, 69(1), 1–15. <https://doi.org/10.1016/j.jappgeo.2009.02.006>

867 Marone, C. J., Scholtz, C. H., & Bilham, R. (1991). On the mechanics of earthquake afterslip.  
868 *Journal of Geophysical Research: Solid Earth*, 96(B5), 8441–8452.  
869 <https://doi.org/10.1029/91JB00275>

870 Maubant, L., Socquet, A., Hollingsworth, J., Pathier, E., & Pousse-Beltrán, L. (2017). The Seismic  
871 Sequence of the Norcia Earthquake, Italy 2016, seen by geodesy. In *Cargese, 2nd of*  
872 *October – 6th of October 2017*. France.

873 Moré, J. J. (1978). The Levenberg-Marquardt algorithm: Implementation and theory. In G. A.  
874 Watson (Ed.), *Numerical Analysis* (pp. 105–116). Springer Berlin Heidelberg.

875 Nielsen, S. B., & Knopoff, L. (1998). The equivalent strength of geometrical barriers to  
876 earthquakes. *Journal of Geophysical Research: Solid Earth*, 103(B5), 9953–9965.  
877 <https://doi.org/10.1029/97JB03293>

878 Noda, H., & Lapusta, N. (2013). Stable creeping fault segments can become destructive as a  
879 result of dynamic weakening. *Nature*, 493(7433), 518–521.  
880 <https://doi.org/10.1038/nature11703>

881 Papadopoulos, G. A., Ganas, A., Agalos, A., Papageorgiou, A., Triantafyllou, I., Kontoes, C., et  
882 al. (2017). Earthquake Triggering Inferred from Rupture Histories, DInSAR Ground  
883 Deformation and Stress-Transfer Modelling: The Case of Central Italy During August  
884 2016–January 2017. *Pure and Applied Geophysics*, 174(10), 3689–3711.  
885 <https://doi.org/10.1007/s00024-017-1609-8>

886 Pavlides, S., Chatzipetros, A., Papathanasiou, G., Georgiadis, G., Sboras, S., & Valkaniotis, S.  
887 (2017). Ground deformation and fault modeling of the 2016 sequence (24 Aug. – 30  
888 Oct.) in central Apennines (Central Italy). *Bulletin of the Geological Society of Greece*,  
889 51(0), 76–112. <https://doi.org/10.12681/bgsg.14334>

890 Perfettini, H., & Avouac, J.-P. (2004). Postseismic relaxation driven by brittle creep: A possible  
891 mechanism to reconcile geodetic measurements and the decay rate of aftershocks,  
892 application to the Chi-Chi earthquake, Taiwan. *Journal of Geophysical Research: Solid*  
893 *Earth*, 109(B2). <https://doi.org/10.1029/2003JB002488>

- 894 Perfettini, H., Avouac, J.-P., Tavera, H., Kositsky, A., Nocquet, J.-M., Bondoux, F., et al. (2010).  
895 Seismic and aseismic slip on the Central Peru megathrust. *Nature*, *465*(7294), 78–81.  
896 <https://doi.org/10.1038/nature09062>
- 897 Perouse, E., Benedetti, L., Fleury, J., Rizza, M., Puliti, I., Billant, J., et al. (2018). Coseismic Slip  
898 Vectors of 24 August and 30 October 2016 Earthquakes in Central Italy: Oblique Slip  
899 and Regional Kinematic Implications. *Tectonics*, *37*(10), 3760–3781.  
900 <https://doi.org/10.1029/2018TC005083>
- 901 Petitta, M., Mastrorillo, L., Preziosi, E., Banzato, F., Barberio, M. D., Billi, A., et al. (2018). Water-  
902 table and discharge changes associated with the 2016–2017 seismic sequence in  
903 central Italy: hydrogeological data and a conceptual model for fractured carbonate  
904 aquifers. *Hydrogeology Journal*, 1–18. <https://doi.org/10.1007/s10040-017-1717-7>
- 905 Pinel-Puységur, B., Michel, R., & Avouac, J.-P. (2012). Multi-link InSAR time series:  
906 Enhancement of a wrapped interferometric database. *IEEE Journal of Selected Topics  
907 in Applied Earth Observations and Remote Sensing*, *5*(3), 784–794.  
908 <https://doi.org/10.1109/JSTARS.2012.2196758>
- 909 Pino, N. A., Convertito, V., & Madariaga, R. (2019). Clock advance and magnitude limitation  
910 through fault interaction: the case of the 2016 central Italy earthquake sequence.  
911 *Scientific Reports*, *9*(1), 5005. <https://doi.org/10.1038/s41598-019-41453-1>
- 912 Pizzi, A., Di Domenica, A., Gallovič, F., Luzi, L., & Puglia, R. (2017). Fault segmentation as  
913 constraint to the occurrence of the main shocks of the 2016 Central Italy seismic  
914 sequence. *Tectonics*, 2017TC004652. <https://doi.org/10.1002/2017TC004652>
- 915 Pluymakers, A. M. H., Niemeijer, A. R., & Spiers, C. J. (2016). Frictional properties of simulated  
916 anhydrite-dolomite fault gouge and implications for seismogenic potential. *Journal of  
917 Structural Geology*, *84*, 31–46. <https://doi.org/10.1016/j.jsg.2015.11.008>
- 918 Pollitz, F. F., Wicks, C., & Thatcher, W. (2001). Mantle Flow Beneath a Continental Strike-Slip  
919 Fault: Postseismic Deformation After the 1999 Hector Mine Earthquake. *Science*,  
920 *293*(5536), 1814–1818. <https://doi.org/10.1126/science.1061361>
- 921 Porreca, M., Minelli, G., Ercoli, M., Brobia, A., Mancinelli, P., Cruciani, F., et al. (2018). Seismic  
922 reflection profiles and subsurface geology of the area interested by the 2016-2017

923 earthquake sequence (Central Italy). *Tectonics*.

924 <https://doi.org/10.1002/2017TC004915>

925 Puliti, I., Pizzi, A., Benedetti, L., Domenica, A. D., & Fleury, J. (2020). Comparing slip distribution

926 of an active fault system at various timescales: insights for the evolution of the Mt.

927 Vettore- Mt. Bove fault system in Central Apennines. *Tectonics*, *n/a(n/a)*,

928 e2020TC006200. <https://doi.org/10.1029/2020TC006200>

929 Rabus, B., Eineder, M., Roth, A., & Bamler, R. (2003). The shuttle radar topography mission—a

930 new class of digital elevation models acquired by spaceborne radar. *ISPRS Journal of*

931 *Photogrammetry and Remote Sensing*, *57(4)*, 241–262.

932 [https://doi.org/10.1016/S0924-2716\(02\)00124-7](https://doi.org/10.1016/S0924-2716(02)00124-7)

933 Ragon, T., Sladen, A., & Simons, M. (2019). Accounting for uncertain fault geometry in

934 earthquake source inversions – II: application to the Mw 6.2 Amatrice earthquake,

935 Central Italy. *Geophysical Journal International*. <https://doi.org/10.1093/gji/ggz180>

936 Rice, J. R. (2006). Heating and weakening of faults during earthquake slip. *Journal of*

937 *Geophysical Research: Solid Earth*, *111*, n/a-n/a.

938 <https://doi.org/10.1029/2005jb004006>

939 Riva, R. E. M., Borghi, A., Aoudia, A., Barzaghi, R., Sabadini, R., & Panza, G. F. (2007). Viscoelastic

940 relaxation and long-lasting after-slip following the 1997 Umbria-Marche (Central Italy)

941 earthquakes. *Geophysical Journal International*, *169(2)*, 534–546.

942 <https://doi.org/10.1111/j.1365-246X.2007.03315.x>

943 Roeloffs, E. (1996). Poroelastic Techniques in the Study of Earthquake-Related Hydrologic

944 Phenomena. In *Advances in Geophysics* (Vol. 37, pp. 135–195). Elsevier.

945 [https://doi.org/10.1016/S0065-2687\(08\)60270-8](https://doi.org/10.1016/S0065-2687(08)60270-8)

946 Rousset, B., Campillo, M., Lasserre, C., Frank, W. B., Cotte, N., Walpersdorf, A., et al. (2017). A

947 geodetic matched filter search for slow slip with application to the Mexico subduction

948 zone: GEODETIC MATCHED FILTER FOR SLOW SLIP. *Journal of Geophysical Research:*

949 *Solid Earth*, *122(12)*, 10,498–10,514. <https://doi.org/10.1002/2017JB014448>

950 Ruina, A. (1983). Slip instability and state variable friction laws. *Journal of Geophysical*  
951 *Research: Solid Earth*, 88(B12), 10359–10370.  
952 <https://doi.org/10.1029/JB088iB12p10359>

953 Scholz, C. H. (1998). Earthquakes and friction laws. *Nature*, 391(6662), 37–42.  
954 <https://doi.org/10.1038/34097>

955 Scognamiglio, L., Tinti, E., Casarotti, E., Pucci, S., Villani, F., Cocco, M., et al. (2018). Complex  
956 fault geometry and rupture dynamics of the Mw 6.5, 2016, October 30th central Italy  
957 earthquake. *Journal of Geophysical Research: Solid Earth*.  
958 <https://doi.org/10.1002/2018JB015603>

959 Scuderi, M. M., & Collettini, C. (2016). The role of fluid pressure in induced vs. triggered  
960 seismicity: insights from rock deformation experiments on carbonates. *Scientific*  
961 *Reports*, 6(1), 24852. <https://doi.org/10.1038/srep24852>

962 Silverii, F., D'Agostino, N., Métois, M., Fiorillo, F., & Ventafridda, G. (2016). Transient  
963 deformation of karst aquifers due to seasonal and multiyear groundwater variations  
964 observed by GPS in southern Apennines (Italy). *Journal of Geophysical Research: Solid*  
965 *Earth*, 121(11), 8315–8337. <https://doi.org/10.1002/2016JB013361>

966 Smeraglia, L., Billi, A., Carminati, E., Cavallo, A., & Doglioni, C. (2017). Field- to nano-scale  
967 evidence for weakening mechanisms along the fault of the 2016 Amatrice and Norcia  
968 earthquakes, Italy. *Tectonophysics*. <https://doi.org/10.1016/j.tecto.2017.05.014>

969 Tarantola, A. (2005). *Inverse Problem Theory and Methods for Model Parameter Estimation*.  
970 Society for Industrial and Applied Mathematics.  
971 <https://doi.org/10.1137/1.9780898717921>

972 Tesson, J., Pace, B., Benedetti, L., Visini, F., Delli Roccoli, M., Arnold, M., et al. (2016). Seismic  
973 slip history of the Pizzalto fault (central Apennines, Italy) using in situ-produced <sup>36</sup>Cl  
974 cosmic ray exposure dating and rare earth element concentrations. *Journal of*  
975 *Geophysical Research: Solid Earth*, 121(3), 2015JB012565.  
976 <https://doi.org/10.1002/2015JB012565>

977 Thomas, M. Y., Avouac, J.-P., & Lapusta, N. (2017). Rate-and-state friction properties of the  
978 Longitudinal Valley Fault from kinematic and dynamic modeling of seismic and aseismic

979 slip. *Journal of Geophysical Research: Solid Earth*, 2016JB013615.  
980 <https://doi.org/10.1002/2016JB013615>

981 Thompson, G. A., & Parsons, T. (2016). Vertical deformation associated with normal fault  
982 systems evolved over coseismic, postseismic, and multiseismic periods. *Journal of*  
983 *Geophysical Research: Solid Earth*, 121(3), 2153–2173.  
984 <https://doi.org/10.1002/2015JB012240>

985 Tung, S., & Masterlark, T. (2018). Delayed poroelastic triggering of the 2016 October Visso  
986 earthquake by the August Amatrice earthquake, Italy. *Geophysical Research Letters*.  
987 <https://doi.org/10.1002/2017GL076453>

988 Valigi, D., Mastrorillo, L., Cardellini, C., Checcucci, R., Di Matteo, L., Frondini, F., et al. (2019).  
989 Springs discharge variations induced by strong earthquakes: the Mw 6.5 Norcia event  
990 (Italy, October 30th 2016). *Rendiconti Online Della Società Geologica Italiana*, 47, 141–  
991 146. <https://doi.org/10.3301/ROL.2019.25>

992 Verdecchia, A., Pace, B., Visini, F., Scotti, O., Peruzza, L., & Benedetti, L. (2018). The Role of  
993 Viscoelastic Stress Transfer in Long-Term Earthquake Cascades: Insights After the  
994 Central Italy 2016–2017 Seismic Sequence. *Tectonics*, 37(10), 3411–3428.  
995 <https://doi.org/10.1029/2018TC005110>

996 Villani, F., Civico, R., Pucci, S., Pizzimenti, L., Nappi, R., De Martini, P. M., et al. (2018). A  
997 database of the coseismic effects following the 30 October 2016 Norcia earthquake in  
998 Central Italy. *Scientific Data*, 5, 180049. <https://doi.org/10.1038/sdata.2018.49>

999 Villani, F., Pucci, S., Civico, R., Martini, P. M. D., Cinti, F. R., & Pantosti, D. (2018). Surface faulting  
1000 of the 30 October 2016 Mw 6.5 central Italy earthquake: detailed analysis of a complex  
1001 coseismic rupture. *Tectonics*, 0(ja). <https://doi.org/10.1029/2018TC005175>

1002 Walters, R. J., Gregory, L. C., Wedmore, L. N. J., Craig, T. J., McCaffrey, K., Wilkinson, M., et al.  
1003 (2018). Dual control of fault intersections on stop-start rupture in the 2016 Central Italy  
1004 seismic sequence. *Earth and Planetary Science Letters*, 500, 1–14.  
1005 <https://doi.org/10.1016/j.epsl.2018.07.043>

1006 Wang, L., Gao, H., Feng, G., & Xu, W. (2018). Source parameters and triggering links of the  
 1007 earthquake sequence in central Italy from 2009 to 2016 analyzed with GPS and InSAR  
 1008 data. *Tectonophysics*. <https://doi.org/10.1016/j.tecto.2018.07.013>

1009 Wesnousky, S. G. (1988). Seismological and structural evolution of strike-slip faults. *Nature*,  
 1010 335(6188), 340. <https://doi.org/10.1038/335340a0>

1011 Xu, G., Xu, C., Wen, Y., & Jiang, G. (2017). Source Parameters of the 2016–2017 Central Italy  
 1012 Earthquake Sequence from the Sentinel-1, ALOS-2 and GPS Data. *Remote Sensing*,  
 1013 9(11), 1182. <https://doi.org/10.3390/rs9111182>

1014 Zhao, B., Bürgmann, R., Wang, D., Tan, K., Du, R., & Zhang, R. (2017). Dominant Controls of  
 1015 Downdip Afterslip and Viscous Relaxation on the Postseismic Displacements Following  
 1016 the Mw7.9 Gorkha, Nepal, Earthquake. *Journal of Geophysical Research: Solid Earth*,  
 1017 122(10), 8376–8401. <https://doi.org/10.1002/2017JB014366>

1018 Zhou, Y., Thomas, M. Y., Parsons, B., & Walker, R. T. (2018). Time-dependent postseismic slip  
 1019 following the 1978 Mw 7.3 Tabas-e-Golshan, Iran earthquake revealed by over 20 years  
 1020 of ESA InSAR observations. *Earth and Planetary Science Letters*, 483, 64–75.  
 1021 <https://doi.org/10.1016/j.epsl.2017.12.005>  
 1022

## 1023 11 References for supplementary materials

1024 Blewitt, G, WC Hammond, and C Kreemer. 2018. “Harnessing the GPS Data Explosion for  
 1025 Interdisciplinary Science.” *Eos* 99. <https://doi.org/10.1029/2018EO104623>.

1026 Boni, CARLO FELICE, CLAUDIA TARRAGONI, LUCIO MARTARELLI, and SIMONA PIERDOMINICI.  
 1027 2010. “STUDIO IDROGEOLOGICO NEL SETTORE NORD-OCCIDENTALE DEI MONTI  
 1028 SIBILLINI: UN CONTRIBUTO ALLA CARTOGRAFIA IDROGEOLOGICA UFFICIALE.” *Italian*  
 1029 *Journal of Engineering Geology and Environment* 2: 16.  
 1030 <https://doi.org/10.4408/IJEGE.2010-02.O-02>.

1031 Cheloni, D., E. Falcucci, and S. Gori. 2019. “Half-Graben Rupture Geometry of the 30 October  
 1032 2016 MW 6.6 Mt. Vettore-Mt. Bove Earthquake, Central Italy.” *Journal of Geophysical*  
 1033 *Research: Solid Earth* 0 (ja). <https://doi.org/10.1029/2018JB015851>.

- 1034 Chiaraluce, L., R. Di Stefano, E. Tinti, L. Scognamiglio, M. Michele, E. Casarotti, M. Cattaneo, et  
1035 al. 2017. "The 2016 Central Italy Seismic Sequence: A First Look at the Mainshocks,  
1036 Aftershocks, and Source Models." *Seismological Research Letters* 88 (3): 757–71.  
1037 <https://doi.org/10.1785/0220160221>.
- 1038 Chiles, Jean-Paul, and Pierre Delfiner. 2009. *Geostatistics: Modeling Spatial Uncertainty*. Vol.  
1039 497. John Wiley & Sons.
- 1040 Grandin, R. 2009. *L'Apport de La Géodésie Spatiale Dans La Compréhension Du Processus de*  
1041 *Rifting Magmatique : L'exemple de l'épisode En Cours En Afar Ethiopien (2005-2009)*.  
1042 Institut de physique du globe (Paris). <http://www.theses.fr/2009GLOB0013>.
- 1043 Hansen, P. 1992. "Analysis of Discrete Ill-Posed Problems by Means of the L-Curve." *SIAM*  
1044 *Review* 34 (4): 561–80. <https://doi.org/10.1137/1034115>.
- 1045 Improta, Luigi, Diana Latorre, Lucia Margheriti, Anna Nardi, Alessandro Marchetti, Anna Maria  
1046 Lombardi, Barbara Castello, et al. 2019. "Multi-Segment Rupture of the 2016 Amatrice-  
1047 Visso-Norcia Seismic Sequence (Central Italy) Constrained by the First High-Quality  
1048 Catalog of Early Aftershocks." *Scientific Reports* 9 (1): 6921.  
1049 <https://doi.org/10.1038/s41598-019-43393-2>.
- 1050 Jolivet, R., C. Lasserre, M.-P. Doin, S. Guillaso, G. Peltzer, R. Dailu, J. Sun, Z.-K. Shen, and X. Xu.  
1051 2012. "Shallow Creep on the Haiyuan Fault (Gansu, China) Revealed by SAR  
1052 Interferometry." *Journal of Geophysical Research: Solid Earth* 117 (B6): B06401.  
1053 <https://doi.org/10.1029/2011JB008732>.
- 1054 Jolivet, R., M. Simons, P. S. Agram, Z. Duputel, and Z.-K. Shen. 2015. "Aseismic Slip and  
1055 Seismogenic Coupling along the Central San Andreas Fault." *Geophysical Research*  
1056 *Letters* 42 (2). <https://doi.org/10.1002/2014GL062222>.
- 1057 Lohman, Rowena B., and Mark Simons. 2005. "Some Thoughts on the Use of InSAR Data to  
1058 Constrain Models of Surface Deformation: Noise Structure and Data Downsampling."  
1059 *Geochemistry, Geophysics, Geosystems* 6 (1): Q01007.  
1060 <https://doi.org/10.1029/2004GC000841>.
- 1061 Maubant, Louise, Anne Socquet, James Hollingsworth, Erwan Pathier, and Pousse Lea. 2017.  
1062 "The Seismic Sequence of the Norcia Earthquake, Italy 2016, Seen by Geodesy." In

1063            *Colloque G2 2017 Géodésie - Rhéologie, 13-15 Nov. 2017 Nice*. France. <https://g2->  
1064            [2017.sciencesconf.org/program](https://g2-2017.sciencesconf.org/program).

1065 Petitta, Marco, Lucia Mastroiello, Elisabetta Preziosi, Francesca Banzato, Marino Domenico  
1066 Barberio, Andrea Billi, Costanza Cambi, et al. 2018. "Water-Table and Discharge  
1067 Changes Associated with the 2016–2017 Seismic Sequence in Central Italy:  
1068 Hydrogeological Data and a Conceptual Model for Fractured Carbonate Aquifers."  
1069 *Hydrogeology Journal*, January, 1–18. <https://doi.org/10.1007/s10040-017-1717-7>.

1070 Pierantoni, Pietro, Giovanni Deiana, and Sandro Galdenzi. 2013. "Stratigraphic and Structural  
1071 Features of the Sibillini Mountains (Umbria-Marche Apennines, Italy)." *Italian Journal*  
1072 *of Geosciences* 132 (3): 497–520. <https://doi.org/10.3301/IJG.2013.08>.

1073 Puliti, I., A. Pizzi, L. Benedetti, A. Di Domenica, and J. Fleury. 2020. "Comparing Slip Distribution  
1074 of an Active Fault System at Various Timescales: Insights for the Evolution of the Mt.  
1075 Vettore- Mt. Bove Fault System in Central Apennines." *Tectonics* n/a (n/a):  
1076 e2020TC006200. <https://doi.org/10.1029/2020TC006200>.

1077 Radiguet, M., F. Cotton, M. Vergnolle, M. Campillo, B. Valette, V. Kostoglodov, and N. Cotte.  
1078 2011. "Spatial and Temporal Evolution of a Long Term Slow Slip Event: The 2006  
1079 Guerrero Slow Slip Event." *Geophysical Journal International* 184 (2): 816–28.  
1080 <https://doi.org/10.1111/j.1365-246X.2010.04866.x>.

1081 Ragon, Théa, Anthony Sladen, and Mark Simons. 2019. "Accounting for Uncertain Fault  
1082 Geometry in Earthquake Source Inversions – II: Application to the Mw 6.2 Amatrice  
1083 Earthquake, Central Italy." *Geophysical Journal International*.  
1084 <https://doi.org/10.1093/gji/ggz180>.

1085 Scognamiglio, L., E. Tinti, E. Casarotti, S. Pucci, F. Villani, M. Cocco, F. Magnoni, A. Michelini,  
1086 and D. Dreger. 2018. "Complex Fault Geometry and Rupture Dynamics of the Mw 6.5,  
1087 2016, October 30th Central Italy Earthquake." *Journal of Geophysical Research: Solid*  
1088 *Earth*. <https://doi.org/10.1002/2018JB015603>.

1089 Sudhaus, Henriette, and Sigurjón Jonsson. 2009. "Improved Source Modelling through  
1090 Combined Use of InSAR and GPS under Consideration of Correlated Data Errors:

1091 Application to the June 2000 Kleifarvatn Earthquake, Iceland.” *Geophysical Journal*  
1092 *International* 176 (2): 389–404. <https://doi.org/10.1111/j.1365-246X.2008.03989.x>.

1093 Tarantola, Albert. 2005. *Inverse Problem Theory and Methods for Model Parameter Estimation*.  
1094 Society for Industrial and Applied Mathematics.  
1095 <https://doi.org/10.1137/1.9780898717921>.

1096 Tarantola, Albert, and Bernard Valette. 1982. “Generalized Nonlinear Inverse Problems Solved  
1097 Using the Least Squares Criterion.” *Reviews of Geophysics* 20 (2): 219.  
1098 <https://doi.org/10.1029/RG020i002p00219>.

1099 Tarquini, Simone, Stefano Vinci, Massimiliano Favalli, Fawzi Doumaz, Alessandro Fornaciai, and  
1100 Luca Nannipieri. 2012. “Release of a 10-m-Resolution DEM for the Italian Territory:  
1101 Comparison with Global-Coverage DEMs and Anaglyph-Mode Exploration via the  
1102 Web.” *Computers & Geosciences* 38 (1): 168–70.  
1103 <https://doi.org/10.1016/j.cageo.2011.04.018>.

1104 Valigi, Daniela, Lucia Mastrorillo, Carlo Cardellini, Roberto Checcucci, Lucio Di Matteo,  
1105 Francesco Frondini, Francesco Mirabella, Stefano Viaroli, and Isotta Vispi. 2019.  
1106 “Springs Discharge Variations Induced by Strong Earthquakes: The Mw 6.5 Norcia Event  
1107 (Italy, October 30th 2016).” *Rendiconti Online Della Società Geologica Italiana* 47  
1108 (March): 141–46. <https://doi.org/10.3301/ROL.2019.25>.

1109 Villani, Fabio, Riccardo Civico, Stefano Pucci, Luca Pizzimenti, Rosa Nappi, Paolo Marco De  
1110 Martini, the Open EMERGEO Working Group, et al. 2018. “A Database of the Coseismic  
1111 Effects Following the 30 October 2016 Norcia Earthquake in Central Italy.” *Scientific*  
1112 *Data* 5 (March): 180049. <https://doi.org/10.1038/sdata.2018.49>.

1113 Wackernagel, Hans. 2003. *Multivariate Geostatistics: An Introduction with Applications*. 3rd  
1114 ed. Berlin Heidelberg: Springer-Verlag. <https://doi.org/10.1007/978-3-662-05294-5>.

1115 Wright, Tim J., Barry E. Parsons, and Zhong Lu. 2004. “Toward Mapping Surface Deformation  
1116 in Three Dimensions Using InSAR.” *Geophysical Research Letters* 31 (1).  
1117 <https://doi.org/10.1029/2003GL018827>.  
1118